

Event Structure and Double Helicity Asymmetry in Jet Production from Polarized
 $p + p$ Collisions at $\sqrt{s} = 200$ GeV

A. Adare,⁹ S. Afanasiev,²³ C. Aidala,¹⁰ N.N. Ajitanand,⁴⁹ Y. Akiba,^{43,44} H. Al-Bataineh,³⁸ J. Alexander,⁴⁹
K. Aoki,^{28,43} L. Aphecetche,⁵¹ R. Armendariz,³⁸ S.H. Aronson,⁴ J. Asai,⁴⁴ E.T. Atomssa,²⁹ R. Averbek,⁵⁰
T.C. Awes,³⁹ B. Azmoun,⁴ V. Babintsev,¹⁹ G. Baksay,¹⁵ L. Baksay,¹⁵ A. Baldisseri,¹² K.N. Barish,⁵ P.D. Barnes,³¹
B. Bassalleck,³⁷ S. Bathe,⁵ S. Batsouli,³⁹ V. Baublis,⁴² A. Bazilevsky,⁴ S. Belikov,^{4,*} R. Bennett,⁵⁰ Y. Berdnikov,⁴⁶
A.A. Bickley,⁹ J.G. Boissevain,³¹ H. Borel,¹² K. Boyle,⁵⁰ M.L. Brooks,³¹ H. Buesching,⁴ V. Bumazhnov,¹⁹
G. Bunce,^{4,44} S. Butsyk,^{31,50} S. Campbell,⁵⁰ B.S. Chang,⁵⁸ J.-L. Charvet,¹² S. Chernichenko,¹⁹ J. Chiba,²⁴
C.Y. Chi,¹⁰ M. Chiu,²⁰ I.J. Choi,⁵⁸ T. Chujo,⁵⁵ P. Chung,⁴⁹ A. Churnin,¹⁹ V. Cianciolo,³⁹ C.R. Clevin,¹⁷
B.A. Cole,¹⁰ M.P. Comets,⁴⁰ P. Constantin,³¹ M. Csanád,¹⁴ T. Csörgő,²⁵ T. Dahms,⁵⁰ K. Das,¹⁶ G. David,⁴
M.B. Deaton,¹ K. Dehmelt,¹⁵ H. Delagrangé,⁵¹ A. Denisov,¹⁹ D. d'Enterria,¹⁰ A. Deshpande,^{44,50} E.J. Desmond,⁴
O. Dietzsch,⁴⁷ A. Dion,⁵⁰ M. Donadelli,⁴⁷ O. Drapier,²⁹ A. Drees,⁵⁰ A.K. Dubey,⁵⁷ A. Durum,¹⁹ V. Dzhordzhadze,⁵
Y.V. Efremenko,³⁹ J. Egdemir,⁵⁰ F. Ellinghaus,⁹ W.S. Emam,⁵ A. Enokizono,³⁰ H. En'yo,^{43,44} S. Esumi,⁵⁴
K.O. Eyser,⁵ D.E. Fields,^{37,44} M. Finger, Jr.,^{6,23} M. Finger,^{6,23} F. Fleuret,²⁹ S.L. Fokin,²⁷ Z. Fraenkel,^{57,*}
J.E. Frantz,⁵⁰ A. Franz,⁴ A.D. Frawley,¹⁶ K. Fujiwara,⁴³ Y. Fukao,^{28,43} T. Fusayasu,³⁶ S. Gadrat,³² I. Garishvili,⁵²
A. Glenn,⁹ H. Gong,⁵⁰ M. Gonin,²⁹ J. Gosset,¹² Y. Goto,^{43,44} R. Granier de Cassagnac,²⁹ N. Grau,²² S.V. Greene,⁵⁵
M. Grosse Perdekamp,^{20,44} T. Gunji,⁸ H.-Å. Gustafsson,^{33,*} T. Hachiya,¹⁸ A. Hadj Henni,⁵¹ C. Haegemann,³⁷
J.S. Haggerty,⁴ H. Hamagaki,⁸ R. Han,⁴¹ H. Harada,¹⁸ E.P. Hartouni,³⁰ K. Haruna,¹⁸ E. Haslum,³³ R. Hayano,⁸
M. Heffner,³⁰ T.K. Hemmick,⁵⁰ T. Hester,⁵ X. He,¹⁷ H. Hiejima,²⁰ J.C. Hill,²² R. Hobbs,³⁷ M. Hohlmann,¹⁵
W. Holzmann,⁴⁹ K. Homma,¹⁸ B. Hong,²⁶ T. Horaguchi,^{43,53} D. Hornback,⁵² T. Ichihara,^{43,44} H. Inuma,^{28,43}
K. Imai,^{28,43} M. Inaba,⁵⁴ Y. Inoue,^{45,43} D. Isenhower,¹ L. Isenhower,¹ M. Ishihara,⁴³ T. Isobe,⁸ M. Issah,⁴⁹
A. Isupov,²³ B.V. Jacak,^{50,†} J. Jia,¹⁰ J. Jin,¹⁰ O. Jinnouchi,⁴⁴ B.M. Johnson,⁴ K.S. Joo,³⁵ D. Jouan,⁴⁰
F. Kajihara,⁸ S. Kametani,^{8,56} N. Kamihara,⁴³ J. Kamin,⁵⁰ M. Kaneta,⁴⁴ J.H. Kang,⁵⁸ H. Kanou,^{43,53} D. Kawal,⁴⁴
A.V. Kazantsev,²⁷ A. Khanzadeev,⁴² J. Kikuchi,⁵⁶ D.H. Kim,³⁵ D.J. Kim,⁵⁸ E. Kim,⁴⁸ E. Kinney,⁹ Á. Kiss,¹⁴
E. Kistenev,⁴ A. Kiyomichi,⁴³ J. Klay,³⁰ C. Klein-Boesing,³⁴ L. Kochenda,⁴² V. Kochetkov,¹⁹ B. Komkov,⁴²
M. Konno,⁵⁴ D. Kotchetkov,⁵ A. Kozlov,⁵⁷ A. Král,¹¹ A. Kravitz,¹⁰ J. Kubart,^{6,21} G.J. Kunde,³¹ N. Kurihara,⁸
K. Kurita,^{45,43} M.J. Kweon,²⁶ Y. Kwon,^{58,52} G.S. Kyle,³⁸ R. Lacey,⁴⁹ Y.S. Lai,¹⁰ J.G. Lajoie,²² A. Lebedev,²²
D.M. Lee,³¹ M.K. Lee,⁵⁸ T. Lee,⁴⁸ M.J. Leitch,³¹ M.A.L. Leite,⁴⁷ B. Lenzi,⁴⁷ T. Liška,¹¹ A. Litvinenko,²³
M.X. Liu,³¹ X. Li,⁷ B. Love,⁵⁵ D. Lynch,⁴ C.F. Maguire,⁵⁵ Y.I. Makdisi,³ A. Malakhov,²³ M.D. Malik,³⁷
V.I. Manko,²⁷ Y. Mao,^{41,43} L. Mašek,^{6,21} H. Masui,⁵⁴ F. Matathias,¹⁰ M. McCumber,⁵⁰ P.L. McGaughey,³¹
Y. Miake,⁵⁴ P. Mikeš,^{6,21} K. Miki,⁵⁴ T.E. Miller,⁵⁵ A. Milov,⁵⁰ S. Mioduszewski,⁴ M. Mishra,²³ J.T. Mitchell,⁴
M. Mitrovski,⁴⁹ A. Morreale,⁵ D.P. Morrison,⁴ T.V. Moukhanova,²⁷ D. Mukhopadhyay,⁵⁵ J. Murata,^{45,43}
S. Nagamiya,²⁴ Y. Nagata,⁵⁴ J.L. Nagle,⁹ M. Naglis,⁵⁷ I. Nakagawa,^{43,44} Y. Nakamiya,¹⁸ T. Nakamura,¹⁸
K. Nakano,^{43,53} J. Newby,³⁰ M. Nguyen,⁵⁰ B.E. Norman,³¹ R. Nouicer,⁴ A.S. Nyanin,²⁷ E. O'Brien,⁴ S.X. Oda,⁸
C.A. Ogilvie,²² H. Ohnishi,⁴³ K. Okada,⁴⁴ M. Oka,⁵⁴ O.O. Omiwade,¹ A. Oskarsson,³³ M. Ouchida,¹⁸
K. Ozawa,⁸ R. Pak,⁴ D. Pal,⁵⁵ A.P.T. Palounek,³¹ V. Pantuev,⁵⁰ V. Papavassiliou,³⁸ J. Park,⁴⁸ W.J. Park,²⁶
S.F. Pate,³⁸ H. Pei,²² J.-C. Peng,²⁰ H. Pereira,¹² V. Peresedov,²³ D.Yu. Peressounko,²⁷ C. Pinkenburg,⁴
M.L. Purschke,⁴ A.K. Purwar,³¹ H. Qu,¹⁷ J. Rak,³⁷ A. Rakotozafindrabe,²⁹ I. Ravinovich,⁵⁷ K.F. Read,^{39,52}
S. Rembeczki,¹⁵ M. Reuter,⁵⁰ K. Reygers,³⁴ V. Riabov,⁴² Y. Riabov,⁴² G. Roche,³² A. Romana,^{29,*} M. Rosati,²²
S.S.E. Rosendahl,³³ P. Rosnet,³² P. Rukoyatkin,²³ V.L. Rykov,⁴³ B. Sahlmueller,³⁴ N. Saito,^{28,43,44} T. Sakaguchi,⁴
S. Sakai,⁵⁴ H. Sakata,¹⁸ V. Samsonov,⁴² S. Sato,²⁴ S. Sawada,²⁴ J. Seele,⁹ R. Seidl,²⁰ V. Semenov,¹⁹ R. Seto,⁵
D. Sharma,⁵⁷ I. Shein,¹⁹ A. Shevel,^{42,49} T.-A. Shibata,^{43,53} K. Shigaki,¹⁸ M. Shimomura,⁵⁴ K. Shoji,^{28,43}
A. Sickles,⁵⁰ C.L. Silva,⁴⁷ D. Silvermyr,³⁹ C. Silvestre,¹² K.S. Sim,²⁶ C.P. Singh,² V. Singh,² S. Skutnik,²²
M. Slunečka,^{6,23} A. Soldatov,¹⁹ R.A. Soltz,³⁰ W.E. Sondheim,³¹ S.P. Sorensen,⁵² I.V. Sourikova,⁴ F. Staley,¹²
P.W. Stankus,³⁹ E. Stenlund,³³ M. Stepanov,³⁸ A. Ster,²⁵ S.P. Stoll,⁴ T. Sugitate,¹⁸ C. Suire,⁴⁰ J. Sziklai,²⁵
T. Tabaru,⁴⁴ S. Takagi,⁵⁴ E.M. Takagui,⁴⁷ A. Taketani,^{43,44} Y. Tanaka,³⁶ K. Tanida,^{43,44,48} M.J. Tannenbaum,⁴
A. Taranenko,⁴⁹ P. Tarján,¹³ T.L. Thomas,³⁷ M. Togawa,^{28,43} A. Toia,⁵⁰ J. Tojo,⁴³ L. Tomášek,²¹ H. Torii,⁴³
R.S. Towell,¹ V.-N. Tram,²⁹ I. Tserruya,⁵⁷ Y. Tsuchimoto,¹⁸ C. Vale,²² H. Valle,⁵⁵ H.W. van Hecke,³¹
J. Velkovska,⁵⁵ R. Vértési,¹³ A.A. Vinogradov,²⁷ M. Virius,¹¹ V. Vrba,²¹ E. Vznuzdaev,⁴² M. Wagner,^{28,43}
D. Walker,⁵⁰ X.R. Wang,³⁸ Y. Watanabe,^{43,44} J. Wessels,³⁴ S.N. White,⁴ D. Winter,¹⁰ C.L. Woody,⁴ M. Wysocki,⁹
W. Xie,⁴⁴ Y.L. Yamaguchi,⁵⁶ A. Yanovich,¹⁹ Z. Yasin,⁵ J. Ying,¹⁷ S. Yokkaichi,^{43,44} G.R. Young,³⁹ I. Younus,³⁷
I.E. Yushmanov,²⁷ W.A. Zajc,¹⁰ O. Zaudtke,³⁴ C. Zhang,³⁹ S. Zhou,⁷ J. Zimányi,^{25,*} and L. Zolin²³

(PHENIX Collaboration)

- ¹Abilene Christian University, Abilene, Texas 79699, USA
- ²Department of Physics, Banaras Hindu University, Varanasi 221005, India
- ³Collider-Accelerator Department, Brookhaven National Laboratory, Upton, New York 11973-5000, USA
- ⁴Brookhaven National Laboratory, Upton, New York 11973-5000, USA
- ⁵University of California - Riverside, Riverside, California 92521, USA
- ⁶Charles University, Ovocný trh 5, Praha 1, 116 36, Prague, Czech Republic
- ⁷China Institute of Atomic Energy (CIAE), Beijing, People's Republic of China
- ⁸Center for Nuclear Study, Graduate School of Science, University of Tokyo, 7-3-1 Hongo, Bunkyo, Tokyo 113-0033, Japan
- ⁹University of Colorado, Boulder, Colorado 80309, USA
- ¹⁰Columbia University, New York, New York 10027 and Nevis Laboratories, Irvington, New York 10533, USA
- ¹¹Czech Technical University, Zikova 4, 166 36 Prague 6, Czech Republic
- ¹²Dapnia, CEA Saclay, F-91191, Gif-sur-Yvette, France
- ¹³Debrecen University, H-4010 Debrecen, Egyetem tér 1, Hungary
- ¹⁴ELTE, Eötvös Loránd University, H - 1117 Budapest, Pázmány P. s. 1/A, Hungary
- ¹⁵Florida Institute of Technology, Melbourne, Florida 32901, USA
- ¹⁶Florida State University, Tallahassee, Florida 32306, USA
- ¹⁷Georgia State University, Atlanta, Georgia 30303, USA
- ¹⁸Hiroshima University, Kagamiyama, Higashi-Hiroshima 739-8526, Japan
- ¹⁹IHEP Protvino, State Research Center of Russian Federation, Institute for High Energy Physics, Protvino, 142281, Russia
- ²⁰University of Illinois at Urbana-Champaign, Urbana, Illinois 61801, USA
- ²¹Institute of Physics, Academy of Sciences of the Czech Republic, Na Slovance 2, 182 21 Prague 8, Czech Republic
- ²²Iowa State University, Ames, Iowa 50011, USA
- ²³Joint Institute for Nuclear Research, 141980 Dubna, Moscow Region, Russia
- ²⁴KEK, High Energy Accelerator Research Organization, Tsukuba, Ibaraki 305-0801, Japan
- ²⁵KFKI Research Institute for Particle and Nuclear Physics of the Hungarian Academy of Sciences (MTA KFKI RMKI), H-1525 Budapest 114, POBox 49, Budapest, Hungary
- ²⁶Korea University, Seoul, 136-701, Korea
- ²⁷Russian Research Center "Kurchatov Institute", Moscow, Russia
- ²⁸Kyoto University, Kyoto 606-8502, Japan
- ²⁹Laboratoire Leprince-Ringuet, Ecole Polytechnique, CNRS-IN2P3, Route de Saclay, F-91128, Palaiseau, France
- ³⁰Lawrence Livermore National Laboratory, Livermore, California 94550, USA
- ³¹Los Alamos National Laboratory, Los Alamos, New Mexico 87545, USA
- ³²LPC, Université Blaise Pascal, CNRS-IN2P3, Clermont-Fd, 63177 Aubiere Cedex, France
- ³³Department of Physics, Lund University, Box 118, SE-221 00 Lund, Sweden
- ³⁴Institut für Kernphysik, University of Muenster, D-48149 Muenster, Germany
- ³⁵Myongji University, Yongin, Kyonggido 449-728, Korea
- ³⁶Nagasaki Institute of Applied Science, Nagasaki-shi, Nagasaki 851-0193, Japan
- ³⁷University of New Mexico, Albuquerque, New Mexico 87131, USA
- ³⁸New Mexico State University, Las Cruces, New Mexico 88003, USA
- ³⁹Oak Ridge National Laboratory, Oak Ridge, Tennessee 37831, USA
- ⁴⁰IPN-Orsay, Université Paris Sud, CNRS-IN2P3, BP1, F-91406, Orsay, France
- ⁴¹Peking University, Beijing, People's Republic of China
- ⁴²PNPI, Petersburg Nuclear Physics Institute, Gatchina, Leningrad region, 188300, Russia
- ⁴³RIKEN Nishina Center for Accelerator-Based Science, Wako, Saitama 351-0198, Japan
- ⁴⁴RIKEN BNL Research Center, Brookhaven National Laboratory, Upton, New York 11973-5000, USA
- ⁴⁵Physics Department, Rikkyo University, 3-34-1 Nishi-Ikebukuro, Toshima, Tokyo 171-8501, Japan
- ⁴⁶Saint Petersburg State Polytechnic University, St. Petersburg, Russia
- ⁴⁷Universidade de São Paulo, Instituto de Física, Caixa Postal 66318, São Paulo CEP05315-970, Brazil
- ⁴⁸Seoul National University, Seoul, Korea
- ⁴⁹Chemistry Department, Stony Brook University, SUNY, Stony Brook, New York 11794-3400, USA
- ⁵⁰Department of Physics and Astronomy, Stony Brook University, SUNY, Stony Brook, New York 11794-3400, USA
- ⁵¹SUBATECH (Ecole des Mines de Nantes, CNRS-IN2P3, Université de Nantes) BP 20722 - 44307, Nantes, France
- ⁵²University of Tennessee, Knoxville, Tennessee 37996, USA
- ⁵³Department of Physics, Tokyo Institute of Technology, Oh-okayama, Meguro, Tokyo 152-8551, Japan
- ⁵⁴Institute of Physics, University of Tsukuba, Tsukuba, Ibaraki 305, Japan
- ⁵⁵Vanderbilt University, Nashville, Tennessee 37235, USA
- ⁵⁶Waseda University, Advanced Research Institute for Science and Engineering, 17 Kikui-cho, Shinjuku-ku, Tokyo 162-0044, Japan
- ⁵⁷Weizmann Institute, Rehovot 76100, Israel
- ⁵⁸Yonsei University, IPAP, Seoul 120-749, Korea

(Dated: November 18, 2021)

We report on the event structure and double helicity asymmetry (A_{LL}) of jet production in longitudinally polarized $p+p$ collisions at $\sqrt{s}=200$ GeV. Photons and charged particles were measured by the PHENIX experiment at midrapidity $|\eta| < 0.35$ with the requirement of a high-momentum (> 2 GeV/ c) photon in the event. Event structure, such as multiplicity, p_T density and thrust in the PHENIX acceptance, were measured and compared with the PYTHIA event generator and the GEANT detector simulation. The shape of jets and the underlying event were well reproduced at this collision energy. For the measurement of jet A_{LL} , photons and charged particles were clustered with a seed-cone algorithm to obtain the cluster p_T sum (p_T^{reco}). The effect of detector response and the underlying events on p_T^{reco} was evaluated with the simulation. The production rate of reconstructed jets is satisfactorily reproduced with the NLO pQCD jet production cross section. For $4 < p_T^{\text{reco}} < 12$ GeV/ c with an average beam polarization of $\langle P \rangle = 49\%$ we measured $A_{LL} = -0.0014 \pm 0.0037^{\text{stat}}$ at the lowest p_T^{reco} bin (4–5 GeV/ c) and $-0.0181 \pm 0.0282^{\text{stat}}$ at the highest p_T^{reco} bin (10–12 GeV/ c) with a beam polarization scale error of 9.4% and a p_T scale error of 10%. Jets in the measured p_T^{reco} range arise primarily from hard-scattered gluons with momentum fraction $0.02 < x < 0.3$ according to PYTHIA. The measured A_{LL} is compared with predictions that assume various $\Delta G(x)$ distributions based on the GRSV parameterization. The present result imposes the limit $-1.1 < \int_{0.02}^{0.3} dx \Delta G(x, \mu^2 = 1\text{GeV}^2) < 0.4$ at 95% confidence level or $\int_{0.02}^{0.3} dx \Delta G(x, \mu^2 = 1\text{GeV}^2) < 0.5$ at 99% confidence level.

PACS numbers: 25.75.Dw

I. INTRODUCTION

The motivation of this measurement is to understand the spin structure of the proton, particularly the contribution of the gluon spin (ΔG) to the proton spin. The proton spin can be represented as

$$\frac{1}{2}_{\text{proton}} = \frac{1}{2} \sum_f \Delta q_f + \Delta G + L_q + L_g, \quad (1)$$

where ΔG is the gluon spin, i.e. the integral of the polarized gluon distribution function, $\Delta G = \int_0^1 dx \Delta G(x)$, $\sum \Delta q$ is the quark spin, and L_q and L_g are the orbital angular momenta of quarks and gluons in the proton. It was found by the EMC experiment at CERN in 1987 that the quark spin contribution to the proton spin is only $(12 \pm 9 \pm 14)\%$ [1, 2]. After the EMC experiment many deep inelastic scattering (DIS) experiments have been carried out to measure $\sum \Delta q$ more precisely. The recent analysis by the HERMES experiment [3] reported that $\sum \Delta q = 0.330 \pm 0.011(\text{theo.}) \pm 0.025(\text{exp.}) \pm 0.028(\text{evol.})$ at a hard-scattering scale $\mu^2 \sim 5$ GeV², which is only about 30% of the proton spin. Consequently, the majority of the proton spin should be carried by the remaining components.

Jet production from longitudinally-polarized $p+p$ collisions is suited for the measurement of ΔG because gluon-involved scatterings, such as $q+g \rightarrow q+g$ or $g+g \rightarrow g+g$, dominate the cross section. The double helicity asymmetry

$$A_{LL} \equiv \frac{\sigma_{++} - \sigma_{+-}}{\sigma_{++} + \sigma_{+-}}, \quad (2)$$

is the asymmetry in cross section between two beam helicity states. In the A_{LL} measurement, many systematic errors cancel out so that high precision can be achieved.

Another motivation of this measurement is to study the event structure of $p+p$ collisions. A high-energy $p+p$ collision produces not only hard scattered partons but also many particles that originate from soft interactions which we call the ‘underlying event’. The PYTHIA event generator phenomenologically models the underlying event on the Multi-Parton Interaction (MPI) scheme [4], and can reproduce the event structure of $p+\bar{p}$ collisions measured by the CDF experiment at $\sqrt{s} = 1.8$ TeV [5]. We present measurements of event structure at lower collision energy, $\sqrt{s} = 200$ GeV, and compare them with those simulated by PYTHIA in order to examine the validity of the PYTHIA MPI scheme. One of the goals of the PHENIX experiment at the Relativistic Heavy Ion Collider (RHIC) is the determination of ΔG . PHENIX has published results on single particle production; the A_{LL} of π^0 production was reported in [6, 7]. This paper reports a measurement of jet production. For ΔG , it is valuable to determine the parton kinematics following the collision in order to better control the x range. In this work we reconstruct jets, observing a larger fraction of the parton’s momentum. This allows improved reconstruction of the original parton kinematics and better statistical accuracy for higher x gluons. Since π^0 s in $p+p$ collisions are produced via jet fragmentation, the measurements of jet and π^0 with same data set have a statistical overlap. The size of the overlap was estimated to be 40-60% depending on the jet p_T . Even in such overlapped events, measured p_T of jets does not correlate with that of π^0 s, and thus the two measurements have an independent sensitivity on x . The fraction of $q+g$ subprocess is larger than $q+q$ and $g+g$ subprocesses in the present jet measurement, making it sensitive to the sign of ΔG . The STAR experiment at RHIC is also measuring inclusive jets to determine ΔG [8]. These measurements

*Deceased

†PHENIX Spokesperson: jacak@skipper.physics.sunysb.edu

have different types of systematic uncertainties and thus one can provide a systematic check for the other.

The remainder of this paper is organized as follows. In Section II, the parts of the PHENIX detector that is relevant to the jet measurement are described. In Section III, analysis methods such as particle clustering and simulation studies are discussed. In Section IV, results on event structure, jet production rate and beam-helicity asymmetries are shown.

II. EXPERIMENTAL SETUP

The PHENIX detector [9] can be grouped into three parts; the Inner Detectors, the Central Arms and the Muon Arms. The schematic drawing of the PHENIX detector is shown in Fig. 1. In this measurement, the Central Arms were used to detect photons and charged particles in jets, and the Inner Detectors to obtain the collision vertex and beam luminosity.

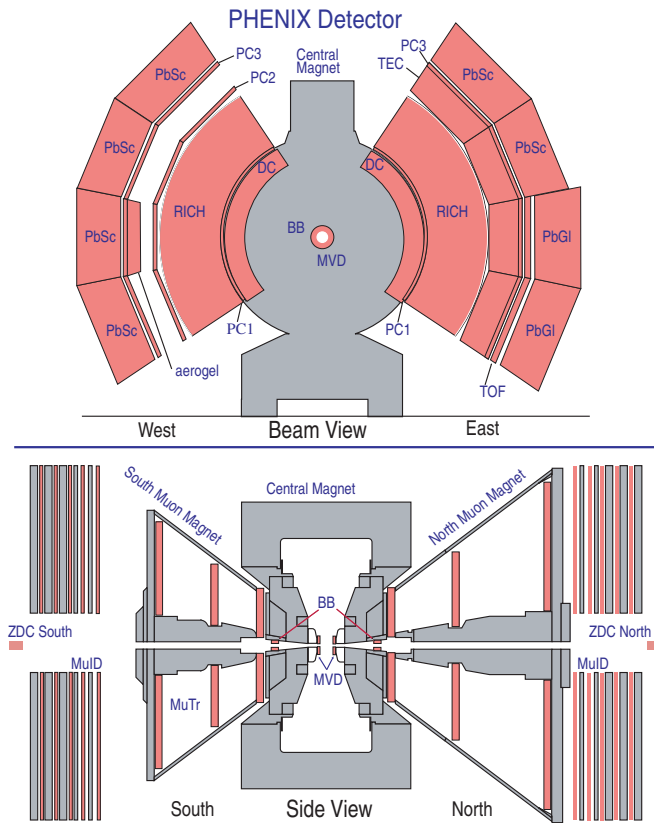


FIG. 1: (color online) PHENIX detector.

A. Inner detectors

The Inner Detectors include the Beam-Beam Counters (BBC) and the Zero-Degree Calorimeters (ZDC).

The BBC is composed of two identical sets of counters placed at both the north and south sides of the collision point with a 144 cm distance [10]. Each counter is composed of 64 sets of PMT plus a 3-cm quartz Čerenkov radiator. The BBC covers a pseudorapidity of $3.0 < |\eta| < 3.9$ over the full azimuth. The BBC measures the number of charged particles in forward and backward regions to determine the collision time, collision z -vertex, and beam luminosity. The timing and z -vertex resolution in $p+p$ collisions are about 100 ps and 2 cm, respectively.

The ZDC is comprised of two sets of hadronic calorimeters placed at the north and south sides of the collision point with a 18 m distance [11]. It covers a $10 \text{ cm} \times 10 \text{ cm}$ area perpendicular to the beam direction, which corresponds to 2.8 mrad when viewed from the collision point. It consists of alternating layers of tungsten absorbers and sampling fibers, and is 150 radiation lengths and 5.1 interaction lengths in depth. It measures neutrons in forward and backward regions and is used as a local polarimeter which assures that the beam polarization is correctly longitudinal or transverse at the interaction region by observing the left-right asymmetry in the $\vec{p}+p \rightarrow \text{neutron} + X$ scattering cross section [12, 13].

B. Central Arms

The Central Arms consist of a tracking system and an electromagnetic calorimeter (EMCal). Pad chambers (PC) and drift chambers (DC) were used to detect charged particles in jets, and the EMCal was used to detect photons in jets.

The EMCal system [14] is located at a distance of 5 m from the interaction point. The system consists of four sectors in each of the East and West Arms, and each sector has a size of $2 \times 4 \text{ m}^2$. The system is composed of two types of calorimeter, lead scintillator (PbSc) and lead glass (PbGl). One PbSc module has a size of $5.5 \times 5.5 \times 37.5 \text{ cm}^3$ corresponding to 18.0 radiation lengths. One PbGl module has a size of $4.0 \times 4.0 \times 40.0 \text{ cm}^3$ corresponding to 14.4 radiation lengths. The energy resolution is $\sim 7\%$ at $E = 1 \text{ GeV}$.

The DC system [15] is located in the region from 2 to 2.4 m from the interaction point to measure the position and momentum of charged particles. The DC system consists of one frame in each of the East and West Arms. Each chamber has a size of $2.5 \text{ m} \times 90^\circ$ in z - ϕ direction with cylindrical shape, and is composed of 80 sense planes with a 2-2.5 cm drift space in the ϕ direction. Each sense plane has 24 wires, which precisely measure r - ϕ position, and 16 tilted wires, which measure z position.

The PC system [15] is composed of multi-wire proportional chambers in three separate layers, which are called PC1, PC2 and PC3, of the Central Arms tracking system. The PC1 is located behind the DC and is used for pattern recognition together with the DC by providing the z coordinate. The PC1 consists of a single plane of anode and field wires lying in a gas volume between two

cathode planes. One cathode is segmented into pixels with a size of $\sim 8.5 \times 8.5 \text{ mm}^2$, and signals from the pixels are read out.

Charged particle tracks are reconstructed using the information from the DC and the PC1 [16]. The magnetic field between the collision vertex and the DC is axial, and thus bends particles in the x - y plane. The field is so weak at the outer area from the DC that particle tracks can be assumed to be straight. A track reconstruction is performed in the DC first, and then reconstructed tracks are associated with hits in the PC1. The momentum resolution is given by σ_p/p (%) = $1.3 \cdot p$ (GeV/ c) \oplus 1.0 for pions.

C. Trigger

The PHENIX experiment has various trigger configurations to efficiently select many type of interesting rare events. This measurement required the coincidence of two triggers; a minimum bias (MB) trigger issued by the BBC, and a high-energy photon trigger issued by the EMCal.

The MB trigger in $p+p$ collisions requires one charged particle in both the north and south sides of the BBC. The reconstructed z -vertex is required to be within $\pm \sim 30$ cm. The efficiency, f_{MB} , of the MB trigger for high- p_T QCD scatterings such as jet production is 0.784 ± 0.020 , which has been determined with the ratio of π^0 yields with and without the MB trigger requirement.

The high-energy photon trigger is fired when the sum of energy deposits in 4×4 EMCal modules ($\Delta\phi \simeq \Delta\eta \simeq 0.04$) is above a threshold, ~ 1.4 GeV, which varies by ~ 0.2 GeV area-by-area due to the variations of gain and threshold between EMCal modules. Each 4×4 area overlaps with others, and thus even when a photon hits the edge of a 4×4 area the next overlapped 4×4 area can gather all energy of the photon. The trigger efficiency is almost flat and close to unity above $E \sim 2$ GeV except masked areas due to noise in the trigger electronics.

III. ANALYSIS METHODS

A. Outline

This analysis used 2.3 pb^{-1} of data that were taken with the MB + high-energy-photon trigger in 2005. In addition, $\sim 0.3 \text{ pb}^{-1}$ of data that were taken with the MB trigger alone were used for systematic error studies. Photons were detected with the EMCal, and charged particles were detected with the DC and PC1. Measured particles in each PHENIX Central Arm were clustered using a cone method to form a ‘reconstructed jet’ and its transverse momentum (p_T^{reco}). Because of the finite size of the acceptance ($|\eta| < 0.35$), the cone size for the particle clustering were set to 0.3 at maximum. This is smaller than the typical cone size, 0.7 raising two issues: First,

a jet in an NLO calculation is usually defined with the same cone size and compared with the measured jet, but this is optimum when both jet energy and cone size are large since the jet spread due to hadronization becomes significant with small jet energy and cone size. Second, such a small cone is more sensitive to quark jets than gluon jets since gluon jets are broader and softer than quark jets. Because of the situation described above, the theory calculation and the simulation evaluations have been organized as follows.

The cross section and the A_{LL} of inclusive jet production were calculated as a function of jet transverse momentum (p_T^{NLO}) within the framework of a next-to-leading-order perturbative QCD (NLO pQCD). This calculation predicted various A_{LL} ’s by assuming various $\Delta G(x)$ distributions.

A simulation with the PYTHIA event generator [4] and the GEANT detector simulation package [17] was performed to understand the effects of the detector response, the underlying events and the jet-definition difference between the measurement and the theory calculation. PYTHIA simulates parton-parton hard scatterings in $p+p$ collisions at leading order (LO) in α_s with phenomenological initial and final-state radiation and hadronization. GEANT simulates the acceptance and response of the PHENIX detector. We define a jet at the partonic level in PYTHIA. The effect of the detector response and the underlying events was evaluated as the statistical relation between the jets defined in PYTHIA and the reconstructed jets. We assume $p_T^{\text{PY}} = p_T^{\text{NLO}}$ within an uncertainty that will be explained in a later section, and then we obtained the relation between the NLO calculation and the measurement.

To confirm that the simulation reproduces well the real data in terms of event structure, namely spatial distribution of particles in an event, quantities sensitive to event structure were measured. Those include particle multiplicity, transverse-momentum density, thrust distribution and jet-production rate. A comparison was made between the real data and the simulation output.

We derive the predictions of the measured A_{LL} by converting the NLO calculation with the relation between p_T^{NLO} and p_T^{reco} . A χ^2 test between the measured and predicted A_{LL} ’s was performed to determine the most-probable ΔG .

The definitions and relations of jets in this measurement are summarized in Tab. I and Fig. 2.

B. Particle Clustering with Cone Method

A jet in one PHENIX Central Arm is constructed with photons and charged particles detected with the EMCal, the DC and the PC1 of the Central Arm. A seed-cone algorithm, described below, is used for the cluster finding.

TABLE I: Definitions of jets adopted in this measurement.

Reconstructed jet (p_T^{reco})	Hadronic jet made with measurable particles after hadronization with a cone size of $R = 0.3$.
jet in PYTHIA (p_T^{PY})	Partonic jet in PYTHIA without cone.
jet in NLO calculation (p_T^{NLO})	Partonic jet in NLO pQCD calc. with a cone size of $\delta = 1.0$.

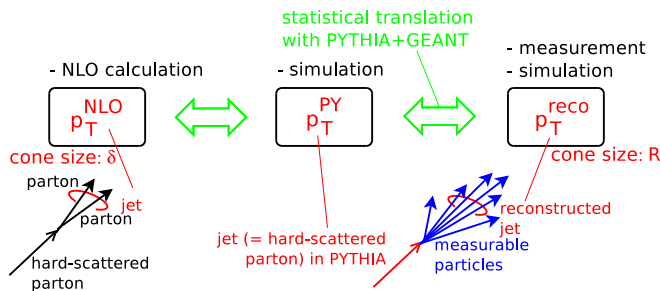


FIG. 2: (color online) Relations between the jets defined in this measurement.

1. Event and particle selections

To select the energy region where the efficiency of the high- p_T photon trigger is in the plateau, at least one photon with $p_T > 2.0$ GeV/ c is required in each event. This requirement causes a bias towards jets that include mostly high- p_T π^0 , η , etc. or radiated photons.

To collect photons from all EMCAL hits, a p_T cut, a charged track veto, and an EMCAL shower shape cut were applied. The p_T cut required the p_T of each EMCAL hit to be > 0.4 GeV/ c in order to eliminate hits likely to be dominated by electronics noise in the detector. It also eliminates charged hadron hits because the measured energy of minimum ionization particles by PbSc peaks at 0.25 GeV. and that of π^\pm with momentum of 1 GeV/ c in the PbGl result in a distribution peaked around 0.4 GeV, with a broad tail to lower energy. The charged track veto reduces charged particle contamination by checking whether each EMCAL hit has a matched charged track within 3σ of their position resolutions. The shower shape cut reduces hadron contamination by comparing the fraction of energy deposits in every EMCAL module of a hit with the fraction predicted by a model of shower shape. This cut eliminates half of hadron hits and statistically 1% of photon hits. These cuts made the contamination of charged and neutral hadrons negligible.

All charged particles detected with the DC and the PC1 were required to have p_T ranging from 0.4 to 4.0 GeV/ c . Below the lower limit, the acceptance is strongly distorted due to a large bending angle and thus becomes shifted from that of photons. The upper limit eliminates fake high- p_T tracks which originate from low- p_T particles

that are produced from a decay or a conversion in the magnetic field. Note that this limit causes a bias towards jets that include fewer charged particles.

2. Cluster finding algorithm

All particles that satisfy the experimental cuts in one arm were used as a seed in cluster finding. Starting with the momentum direction of a seed particle as a temporary cone axis, we calculated the next temporary cone axis with particles which are in the cone. The distance between the cone axis (η^C, ϕ^C) and the momentum direction of each particle (η^i, ϕ^i) is defined as

$$R^i \equiv \sqrt{(\eta^i - \eta^C)^2 + (\phi^i - \phi^C)^2}. \quad (3)$$

The cone radius R was set to 0.3, which was about a half of the η acceptance of the detector. The next temporary cone axis \vec{e}_{next} is calculated as a vector sum of momenta of particles in the cone:

$$\vec{e}_{\text{next}} \equiv \frac{\vec{p}^{\text{reco}}}{|\vec{p}^{\text{reco}}|}, \quad \vec{p}^{\text{reco}} \equiv \sum_{i \in \text{cone}} \vec{p}_i. \quad (4)$$

This procedure was iterated until the temporary cone axis became stable.

The cluster finding is done with all seed particles, and then each seed particle has one cone and some cones can be the same or overlapped. The cone which has the largest p_T^{reco} in an event is used in the event. For measurements of event structure we also define the sum of momenta of all particles in one arm:

$$\vec{p}^{\text{sum}} \equiv \sum_{i \in \text{arm}} \vec{p}_i. \quad (5)$$

An evaluation of p_T^{reco} without seed has been done using a part of the statistics in order to check the effect of the use of a seed. Every direction in the (η, ϕ) space with a step of $\delta\eta = \delta\phi = 0.01$ within the Central Arm acceptance has been used as an initial cone direction in each event. All steps except the choice of the initial cone directions is the same as the original algorithm. The yield of reconstructed jets with the seedless method was larger than that with the seed method by $\sim 20\%$ at $p_T^{\text{reco}} = 4$ GeV/ c , $\sim 10\%$ at $p_T^{\text{reco}} = 8$ GeV/ c and $\sim 5\%$ at $p_T^{\text{reco}} = 12$ GeV/ c . This deviation is compensated in the relation between p_T^{reco} and p_T^{PY} estimated with the simulation, and therefore the p_T^{reco} difference between the two methods of cluster finding is smaller than the deviation above.

C. Simulation Study

1. Simulation settings

The PYTHIA version 6.220 was used. Only QCD high- p_T processes were generated by setting the process switch

(“MSEL”) to 1 and the lower cutoff of partonic transverse momentum (“CKIN(3)”) to 1.5 GeV/ c . The parameter modification reduces the time for event generation and does not affect any physics results in the measured p_T region, as it has been confirmed by comparing p_T^{reco} distribution etc. to those without the parameter modification. We call a PYTHIA simulation with these conditions ‘PYTHIA default’. Hadron-hadron collisions have a so-called ‘underlying event’, which comes from the breakup of the incident nucleons. The PYTHIA simulation reproduces the underlying event with the Multi-Parton Interaction (MPI) mechanism. The CDF experiment at the Tevatron showed that the PYTHIA simulation did not reproduce the event structure well and modeled a set of tuned parameters called ‘tune A’ [5, 18]. Modified or important parameters are listed in Tab. II.

TABLE II: Important or modified (Used) parameters in the PYTHIA MPI setting.

Parameter	Default	Used	Note
MSTP(81)	1	1	MPI master switch.
MSTP(82)	1	4	double-Gaussian matter distribution used.
PARP(82)	1.9	2.0	turn-off p_T for MPI at the reference energy scale PARP(89)
PARP(83)	0.5	0.5	the fraction of the core Gaussian matter to total hadronic matter
PARP(84)	0.2	0.4	the radius of the core Gaussian matter
PARP(85)	0.33	0.9	the probability that two gluons are produced in MPI with colors connecting to nearest neighbors
PARP(86)	0.66	0.95	the probability that two gluons are produced in MPI with the PARP(85) condition or as a closed loop
PARP(89)	1000	1800	reference energy scale for the turn-off p_T
PARP(90)	0.16	0.25	energy dependence of the turn-off p_T
PARP(67)	1.0	4.0	hard-scattering scale μ^2 multiplied by this sets the maximum parton virtuality in initial-state radiation
MSTP(51)	7	7	CTEQ 5L PDF used.
MSTP(91)	1	1	Gaussian k_T used.
PARP(91)	1.0	1.0	width of k_T distribution.
PARP(93)	5.0	5.0	upper cutoff for k_T dist.

We call a PYTHIA simulation with the tune-A setting ‘PYTHIA MPI’, although it has been adopted as default values in the PYTHIA version 6.226 and later.

We use the output of the ‘PYTHIA default’ and the ‘PYTHIA MPI’ simulations to estimate the effect of the

underlying event on our measurement.

The PHENIX experiment has developed its own GEANT3-based detector simulator, called the Phenix Integrated Simulation Application. The absolute scale and the resolution of the EMCal energy and the tracking momentum have been tuned in the simulation using mass distributions of π^0 (2γ), π^\pm , K^\pm and p^\pm .

2. Relation between p_T^{reco} and p_T^{PY}

The PYTHIA+GEANT simulation was used to evaluate the effect of the detector response and the underlying event on the p_T^{reco} measurement. The p_T of a jet in PYTHIA, which is represented by p_T^{PY} in this paper, should be defined so that it is comparable with the theoretical jet in order to evaluate the relation between the NLO calculation and the measurement. The event-by-event transition from the jet in PYTHIA (p_T^{PY}) to the reconstructed jet (p_T^{reco}) is simulated to obtain the statistical relation between them.

A jet in PYTHIA is defined as a hard-scattered parton that has not undergone final-state parton splits, namely particle number 7 or 8 in the PYTHIA event list. A simulated reconstructed jet is associated with one of the two partons by minimizing the angle $\Delta R = \sqrt{\Delta\eta^2 + \Delta\phi^2}$. Figure 3 shows the ratio $p_T^{\text{reco}}/p_T^{\text{PY}}$ at each p_T^{reco} bin, and Fig. 4 shows the mean value of the ratios as a function of p_T^{reco} . The ratio of the PYTHIA MPI output is $\sim 80\%$ on average and is larger than that of the PYTHIA default output due to the contribution from the underlying event.

The relation between reconstructed jets and jets in PYTHIA can be characterized by multiple effects. Some particles in a jet can leak from the cone because of the limited acceptance, the small cone size and the absence of a detector for neutral hadrons. Some particles produced by the underlying event can be included in the cone and contaminate p_T^{reco} , and thus the ratio $p_T^{\text{reco}}/p_T^{\text{PY}}$ can exceed one. The p_T^{PY} of events that are in a p_T^{reco} bin is distributed widely due to the finite p_T resolution of the PHENIX Central Arm. Because a gluon jet is softer and broader than quark jet [19, 20], the high- p_T photon requirement has lower efficiency for gluon jets. Therefore the ratio of p_T^{reco} to p_T^{PY} for gluon jets is smaller than quark jets on average.

Figure 5 shows the relative yields of quark+quark ($q+q$), quark+gluon ($q+g$) and gluon+gluon ($g+g$) subprocesses as a function of p_T^{PY} at each p_T^{reco} bin. Figure 6 shows the fraction of $g+g$, $q+g$ and $q+q$ subprocesses as a function of p_T^{reco} . These were evaluated with the simulation. As explained above, the gg subprocess is suppressed in this measurement. The dominant subprocess is $q+g$ throughout the p_T^{reco} range.

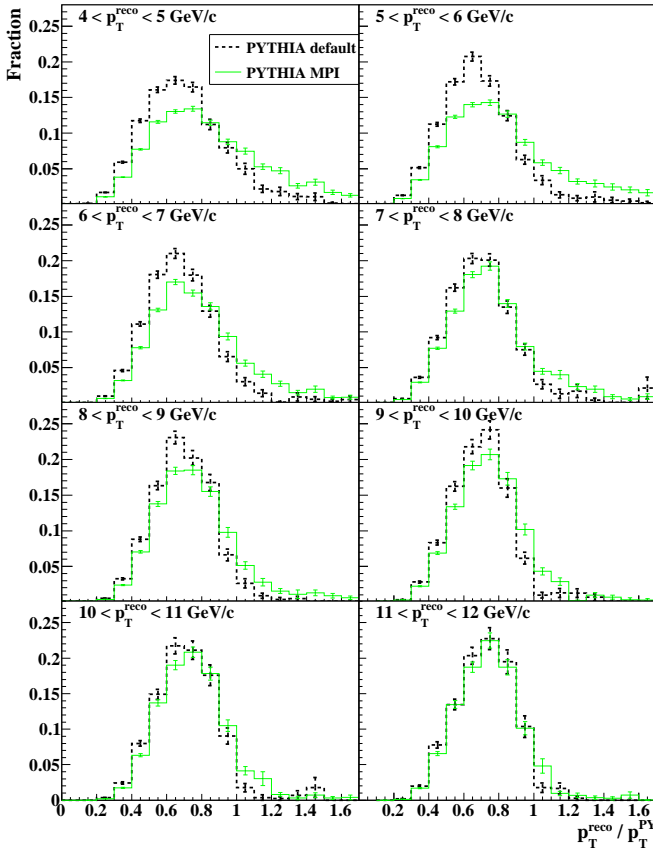


FIG. 3: (color online) Distributions of the ratio $p_T^{\text{reco}}/p_T^{\text{PY}}$ evaluated with (dashed black) PYTHIA default and (solid green) PYTHIA MPI.

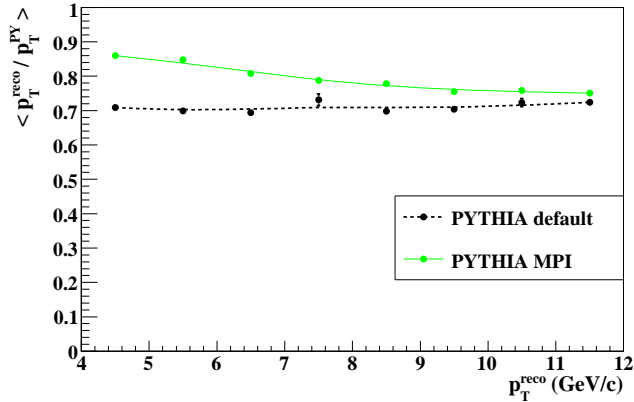


FIG. 4: (color online) The mean value of ratio $p_T^{\text{reco}}/p_T^{\text{PY}}$ as functions of p_T^{reco} .

3. Relation between p_T^{PY} and p_T^{NLO}

The cross section and the A_{LL} of inclusive jet production in $|\eta| < 0.35$ at $\sqrt{s} = 200$ GeV were calculated within the NLO pQCD framework with the CTEQ6M unpolarized PDF under the Small Cone Approximation (SCA) [21–23]. We adopted a cone size of $\delta = 1.0$ for reasons that will be explained in a later section. Figure

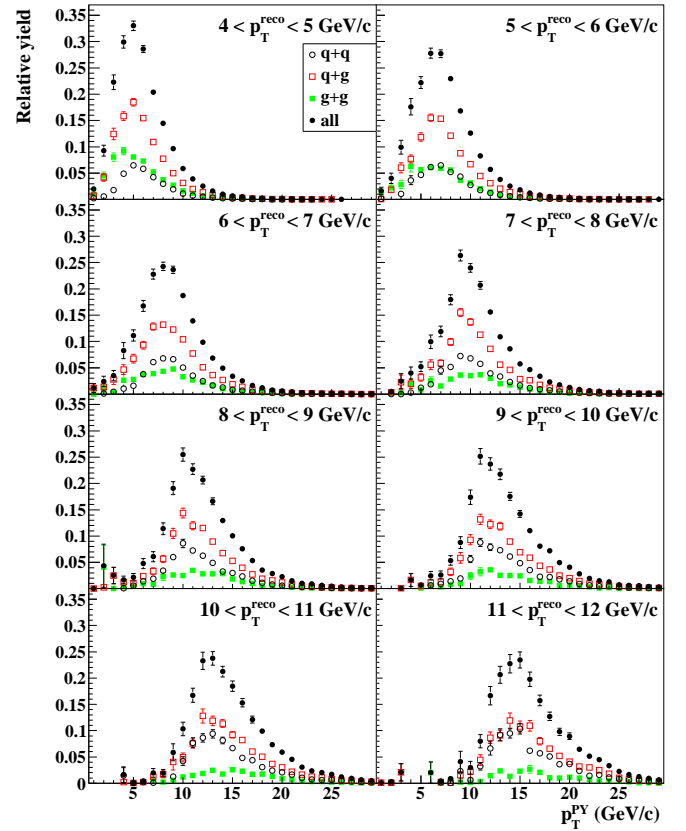


FIG. 5: (color online) The relative yields of $q + q$, $q + g$ and $g + g$ subprocesses in the PYTHIA+GEANT simulation. The results with all the subprocesses combined are also shown.

7 shows the cross section calculated with three factorization scales, $\mu = p_T$, $2p_T$ and $p_T/2$ in NLO pQCD.

The p_T^{NLO} needs to be connected with p_T^{PY} in order to evaluate the relation between the NLO calculation and the measurement, where the relation between p_T^{PY} and p_T^{reco} was obtained from the PYTHIA+GEANT simulation. We assume $p_T^{\text{PY}} = p_T^{\text{NLO}}$, and thus the relation between the jet in PYTHIA and the measurement can be interpreted as the relation between the NLO calculation and the measurement. However the definition of p_T^{PY} and p_T^{NLO} has a discrepancy, and they become close to each other only as the cone half-aperture (δ) in the theory becomes large. Therefore we set δ to 1.0, which is the upper limit where the SCA is applicable, and evaluated the discrepancy between p_T^{PY} and p_T^{NLO} with $\delta = 1.0$ as described later. Moreover, the cone size of the jet in the NLO calculation needs to be larger than the acceptance of the PHENIX Central Arm so that one jet per central arm per event can be reconstructed and connected with the jet in the NLO calculation. This has been also satisfied with the use of $\delta = 1.0$.

Note that the cone size in theory and measurement are different parameters and the difference is compensated for with the PYTHIA simulation; the former is related to

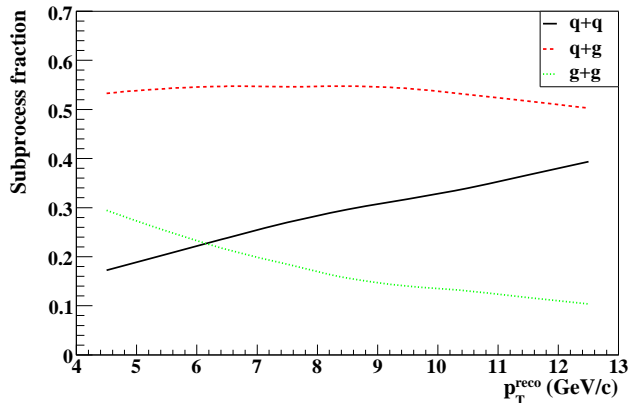


FIG. 6: (color online) Subprocess fractions of reconstructed jets as functions of p_T . It was evaluated with the PYTHIA MPI and GEANT simulation. It should be noted that the gluon-quark reaction is the dominant reaction in all the momentum region from 4 to 12 GeV/c.

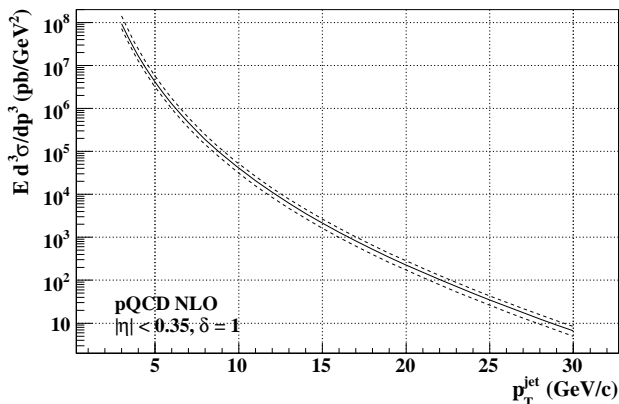


FIG. 7: Unpolarized jet cross section at a pseudorapidity $|\eta| < 0.35$ with a cone half-aperture $\delta = 1$. It was calculated at NLO under the SCA with three factorization scales, $\mu = p_T$ (solid line), $2p_T$ (lower dashed line) and $p_T/2$ (upper dashed line).

the angle between two splitting partons and the latter is related to the angle between stable particles.

4. Uncertainty due to difference in jet definitions

The uncertainty due to the jet-definition difference between the PYTHIA and NLO calculations with $\delta = 1.0$ has been evaluated using the difference between two jet definitions in PYTHIA. One definition is the jet in PYTHIA defined above. The other assumes a cluster of partons with a cone size of $\delta = 1.0$ in PYTHIA, where partons originating from the underlying event are excluded. For the latter definition the jet p_T is denoted $p_T^{\text{in cone}}$. Since $p_T^{\text{in cone}}$ and p_T^{NLO} are defined similarly, i.e. both at the partonic level and with the same cone size δ , we assume

that the scales of $p_T^{\text{in cone}}$ and p_T^{NLO} are the same. Then the difference between $p_T^{\text{in cone}}$ and p_T^{PY} , which can be evaluated using PYTHIA, is considered to be the difference between p_T^{NLO} and p_T^{PY} .

Figure 8 shows distributions of the fraction $p_T^{\text{in cone}}/p_T^{\text{PY}}$ at three typical p_T^{PY} bins. This indicates that the p_T scales of the two jet definitions have a 10% difference on average in the p_T range of these measurements. Therefore the uncertainty due to the jet-definition difference between PYTHIA and the NLO calculation with $\delta = 1.0$ has been assigned 10% in p_T scale.

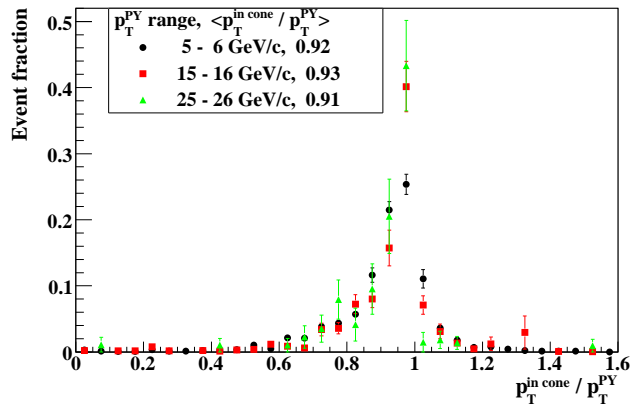


FIG. 8: (color online) Distributions of the fraction $p_T^{\text{in cone}}/p_T^{\text{PY}}$ evaluated with a PYTHIA simulation at three typical p_T^{PY} bins.

5. Reproducibility Check

Figure 9 shows the distribution of p_T^{reco} measured with the clustering method described above. The simulation outputs have been normalized so that they match the real data at $p_T \sim 8$ GeV/c. The slope of the PYTHIA MPI output agrees better with that of the real data, where that of the PYTHIA default output is less steep. The relative yield between the real data and the PYTHIA MPI output is consistent within $\pm 10\%$ over five orders of magnitude.

Figure 10 shows distributions of the fraction $p_T^{\text{trig}\gamma}/p_T^{\text{reco}}$, where $p_T^{\text{trig}\gamma}$ is p_T of the trigger photon. The lower cutoff of the distributions is due to the minimum p_T of the trigger photon (> 2 GeV/c). The rightmost bin ($p_T^{\text{trig}\gamma}/p_T^{\text{reco}} \sim 1$) contains events in which only a trigger photon exists. Such events can occur by the limited acceptance, by the EMCAL masked area (particles except a trigger photon in jet are not detected), by EMCAL noise or by direct photon events. The difference between the real data and the simulation outputs in the rightmost bin may indicate that these effects are not completely reproduced by the simulation, but the difference is small ($< 5\%$) and negligible in comparison with other uncertainties.

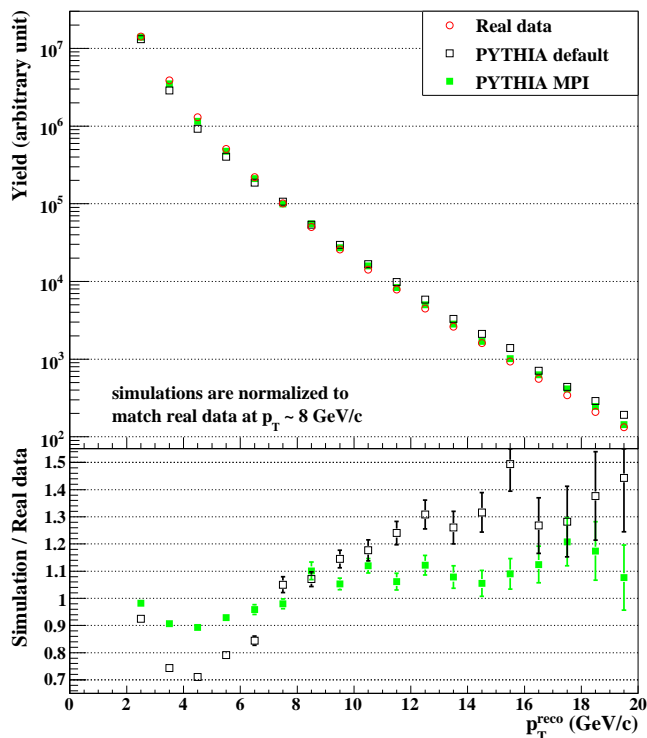


FIG. 9: (color online) Reconstructed-jet yields as a function of p_T^{reco} . The red, black and green points correspond to the real data, the PYTHIA default output and the PYTHIA MPI output, respectively. The simulation outputs have been normalized so that they match the real data at $p_T = 8$ GeV/c. The ratio of the yields between the simulations and the real data is shown at bottom.

IV. RESULTS AND DISCUSSIONS

A. Event structure

1. Multiplicity

Multiplicity is defined as the number of particles which satisfy the experimental cuts in one event. Figure 11(a) and (b) show the mean value of multiplicity in the Central Arm vs p_T^{sum} and in the cluster vs p_T^{reco} . The multiplicities in the arm and in the cluster of the simulation outputs agree, on the whole, with that of the real data. The PYTHIA MPI output is larger than the PYTHIA default output as expected, and the real data are closer to the PYTHIA default output. On the other hand, the p_T^{reco} distributions (Fig. 9) shows better agreement between the real data and the PYTHIA MPI output. This indicates that the PYTHIA MPI reproduces the sum of p_T of particles well, which is less sensitive to particle fragmentation process, while it does not reproduce the particle multiplicity very well. The reproducibility of the summed p_T is checked in measurements described later.

Figure 11(c) and (d) show the ratio of charged-particle multiplicity to photon multiplicity in the Central Arm

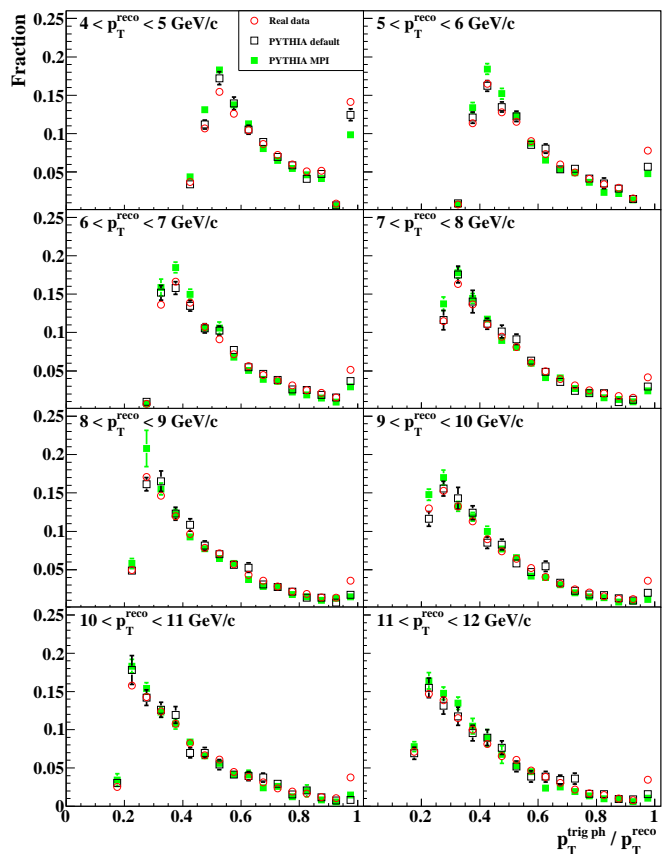


FIG. 10: (color online) The fraction of p_T of the trigger photon in each p_T^{reco} .

and in the cluster. The real data lies below the PYTHIA default and MPI results for both multiplicities. This indicates that the effect of the underlying event in the ratios is small, and the difference between the real data and the PYTHIA results is mainly caused by the imbalance between photons and charged particles in jet. Figure 11(e) and (f) show the ratio of the sum of charged-particle p_T to the sum of photon p_T . These have the same tendency as the multiplicity ratios.

2. Transverse momentum density

The p_T density, $\mathcal{D}_{p_T}(\Delta\phi)$, is defined as

$$\mathcal{D}_{p_T}(\Delta\phi) \equiv \left\langle \frac{1}{\delta\phi} \sum_{i \in [\Delta\phi, \Delta\phi + \delta\phi]} p_{Ti} \right\rangle_{\text{event}}, \quad (6)$$

where $\Delta\phi$ is ϕ angle with respect to the direction of a trigger photon in event, $\delta\phi$ is an area width in ϕ direction, and p_{Ti} is transverse momentum of i -th particle in event. The p_T density means the area-normalized total transverse momentum in an area of $\delta\phi \times \delta\eta$ at a distance $\Delta\phi$ from trigger photon, where $\delta\eta$ is the width of the Central Arm acceptance.

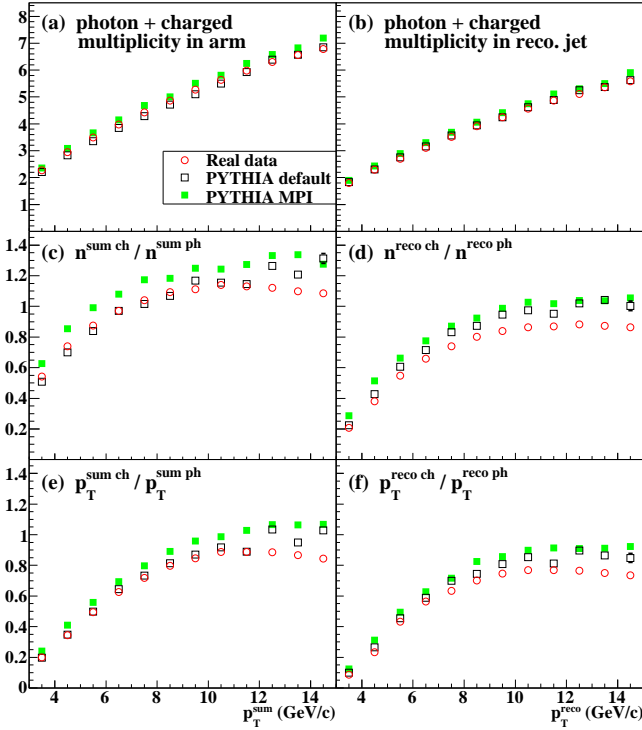


FIG. 11: (color online) (a): Mean multiplicity in the Central Arm vs p_T^{sum} . (b): Mean multiplicity in the cluster vs p_T^{reco} . (c): The ratio of charged multiplicity to photon multiplicity in the Central Arm. (d): Same as (c) but in the cluster. (e): The ratio of charged p_T to photon p_T in the Central Arm. (f): Same as (e) but in the cluster.

We name the region at $\Delta\phi \lesssim 0.7$ rad the ‘toward’ region and the region at $\Delta\phi \gtrsim 0.7$ rad the ‘transverse’ region. Since particles from a jet are concentrated along the jet direction, the \mathcal{D}_{p_T} in the transverse region is sensitive to the underlying event.

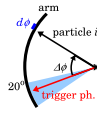


FIG. 12: (color online) Measurement condition of the p_T density. The arc and the \times mark represent one Central Arm and the collision point in the beam view.

As illustrated in Fig. 12, to avoid the effect of the PHENIX Central Arm acceptance in the calculation of \mathcal{D}_{p_T} , we limited the ϕ direction of the trigger photons to less than 20° from one edge of the PHENIX Central Arms, and we did not use photons and charged particles which were in the ϕ area between the trigger photon and the near edge. With this method the \mathcal{D}_{p_T} distribution is not affected by the finite acceptance of the PHENIX

Central Arms up to 70° (~ 1.2 rad).

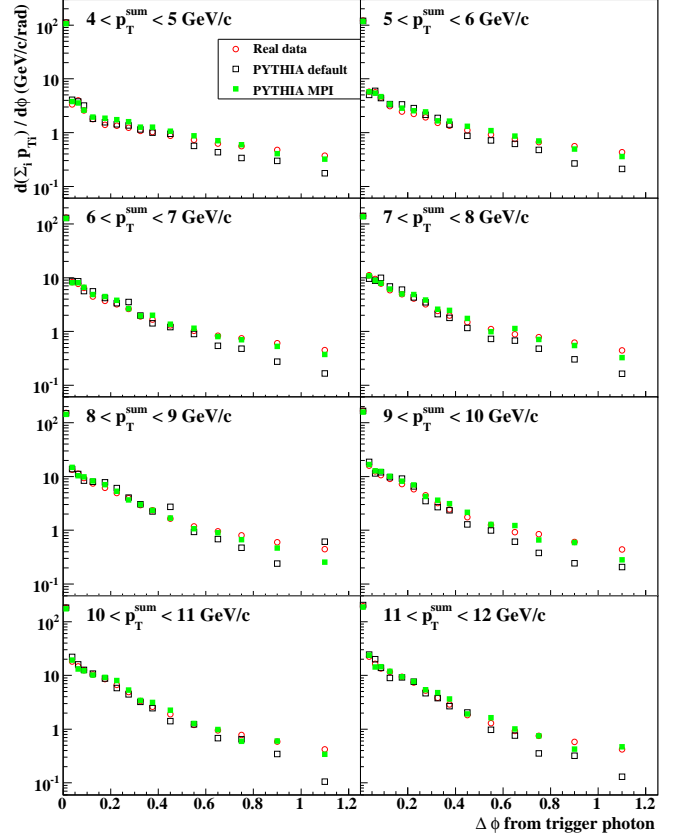


FIG. 13: (color online) p_T density, $\mathcal{D}_{p_T} = d\Sigma_i p_{T_i}/d\phi$ (GeV/c/rad), in each p_T^{sum} bin. Trigger photons are included in the leftmost points.

Figure 13 shows the \mathcal{D}_{p_T} distributions for each p_T^{sum} range. In the ‘‘toward’’ region, the simulation outputs agree well with the real data. It shows that the shape of jets produced by the simulation is consistent with the real data. In the ‘‘transverse’’ region, the PYTHIA default output is generally smaller than the real data. This is an indication that the PYTHIA default does not contain sufficient total p_T of soft particles from the underlying event. The PYTHIA MPI output agrees with the real data well.

3. Thrust distribution in PHENIX Central Arm

We evaluated the thrust variable defined in the CERN-ISR era with particles in one PHENIX Central Arm ($\Delta\eta = 0.7$, $\Delta\phi = 90^\circ$):

$$T_{PH} \equiv \max_{\mathbf{u}} \frac{\sum_i |\mathbf{p}_i \cdot \mathbf{u}|}{\sum_i |\mathbf{p}_i|} = \frac{\sum_i |\mathbf{p}_i \cdot \hat{\mathbf{p}}|}{\sum_i |\mathbf{p}_i|} \quad (7)$$

$$\hat{\mathbf{p}} = \frac{\sum_i \mathbf{p}_i}{|\sum_i \mathbf{p}_i|}, \quad (8)$$

where \mathbf{u} is a unit vector which is called the thrust axis and is directed to maximize T , and \mathbf{p}_i is a momentum of each particle in one arm. If only particles in a half sphere in an event are used, T_{PH} can be written as the right-side formula in Eq. 7.

The distribution of T_{PH} of isotropic events in the PHENIX Central Arm acceptance for each p_T^{sum} bin was simulated with the following method. First, the cross section of inclusive particle production is assumed to be proportional to $\exp(-6 p_T(\text{GeV}/c))$ and is independent of η and ϕ . Second, the same cuts as the experimental conditions are applied numerically: the geometrical acceptance ($|\eta| < 0.35$, $\Delta\phi = 90^\circ$), the momentum limit ($p_T > 0.4\text{GeV}/c$), and one high- p_T particle ($p_T > 2.0\text{GeV}/c$). Third, the distribution of T_{PH} of isotropic events was calculated for each number of particles in one event ($f_n(T)$ for $n = 1, 2, 3, \dots$). The T_{PH} distribution of $n = 2$ events is particularly steep. Thus we applied a cut of $n \geq 3$ in the T_{PH} measurement. The f_T is evaluated as the sum of $f_n(T)$'s weighted by the probability (ϵ_n) that the number of particles per event is n :

$$f(T) = \sum_n \epsilon_n f_n(T) \quad , \quad \epsilon_n = \frac{N_{\text{evt}}^n}{N_{\text{evt}}} \quad (9)$$

where ϵ_n was derived from the real data.

Figure 14 shows the T_{PH} distribution in each p_T^{sum} range. The PYTHIA MPI output agrees with the real data well. The PYTHIA default has a steeper slope, which indicates that the number of particles in the vicinity of jets in the PYTHIA default is insufficient. In the real data, the PYTHIA default output and the PYTHIA MPI output, the T_{PH} distribution becomes sharper as p_T^{sum} increases. This is due to the fact that the transverse momentum (j_T) of a jet is independent of its longitudinal momentum and is almost constant.

If the real data includes a contribution from non-jet (isotropic) events, the T_{PH} distribution of the real data is a mixture of the distribution of the simulation output and the distribution of the isotropic case. The contribution from non-jet events can be judged to be negligible because the PYTHIA MPI output reproduces the data even though it does not have isotropic events.

B. Jet production rate

1. Evaluation method (measurement)

The jet production rate \mathcal{Y} , namely the yield of reconstructed jets per unit luminosity, is defined with measured quantities as

$$\mathcal{Y}^i \equiv \frac{N_{\text{reco}}^i}{L \cdot f_{\text{MB}} \cdot f_{ph}}, \quad (10)$$

where L is the integrated luminosity; f_{MB} and f_{ph} are the efficiencies of the MB trigger (see Sec. II C) and

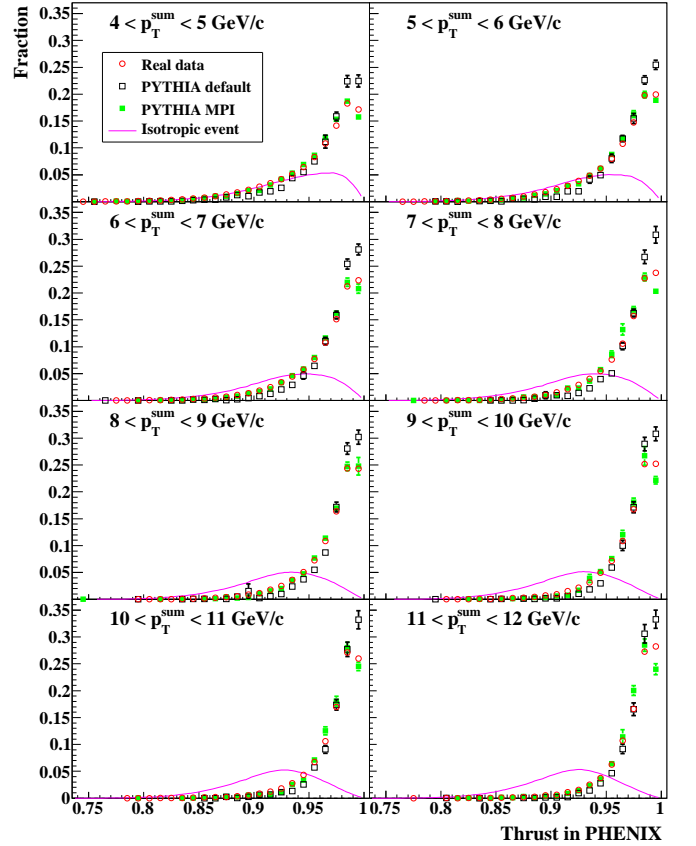


FIG. 14: (color online) T_{PH} distribution in each p_T^{sum} bin. All distributions have been normalized so that their areas were equal to one another. The purple lines are the distributions of isotropic events in the acceptance of the PHENIX Central Arms, which are evaluated with Eq. 9.

the high- p_T photon trigger, respectively; N_{reco}^i is the reconstructed-jet yield in a i -th p_T^{reco} bin. The high- p_T photon trigger efficiency f_{ph} was estimated to be 0.92 ± 0.02 , where the inefficiency is caused by the 10% of the EMCAL acceptance where the trigger was disabled due to electronics noise. The inefficiency is slightly smaller than the disabled acceptance because a particle cluster can contain multiple high- p_T photons.

2. Evaluation method (prediction)

On the other hand, the variable \mathcal{Y} is expressed with theoretical and simulation quantities as

$$\mathcal{Y}^i \equiv \sum_j f^{ij} \cdot \epsilon_{\text{trig+acc}}^j \cdot \mathcal{Y}_{\text{theo}}^j, \quad (11)$$

where the label i and j are the indices of p_T^{reco} and p_T^{NLO} bins, respectively. The $\mathcal{Y}_{\text{theo}}^j$ is a jet production rate within $|\eta| < 0.35$ in a j -th p_T^{NLO} bin, which is theoretically calculated. The $\epsilon_{\text{trig+acc}}^j$ is a high- p_T -photon trigger efficiency and acceptance correction, which is evaluated

with the PYTHIA+GEANT simulation. The $\epsilon_{trig+acc}^j \cdot \mathcal{Y}_{theo}^j$ is a yield of jets that include a high- p_T photon within $|\eta| < 0.35$. The f^{ij} is the probability that a jet within a j -th p_T^{NLO} bin is detected as a reconstructed jet within a i -th p_T^{reco} bin. This method uses the relative p_T^{reco} distribution in each p_T^{NLO} bin and thus the slope of the p_T^{PY} distribution in the simulation does not affect the result of \mathcal{Y}^i .

The correction factor $\epsilon_{trig+acc}^j$ is a fraction, whose numerator is the number of events in which at least one photon with $p_T > 2$ GeV/ c is detected, and whose denominator is the number of events in which jets are in $|\eta| < 0.35$. The condition “ $p_T > 2$ GeV/ c ” in the numerator corrects a high- p_T photon efficiency, i.e. the probability that a high- p_T photon in jets must be detected with the EMCAL. The condition “ $|\eta| < 0.35$ ” in the denominator and the absence of it in the numerator corrects an acceptance for jets, i.e. the fact that a part of reconstructed-jets does originate from jets with $|\eta| > 0.35$. Figure 15 shows $\epsilon_{trig+acc}^j$ as a function of p_T^{NLO} estimated with the PYTHIA default and MPI simulations.

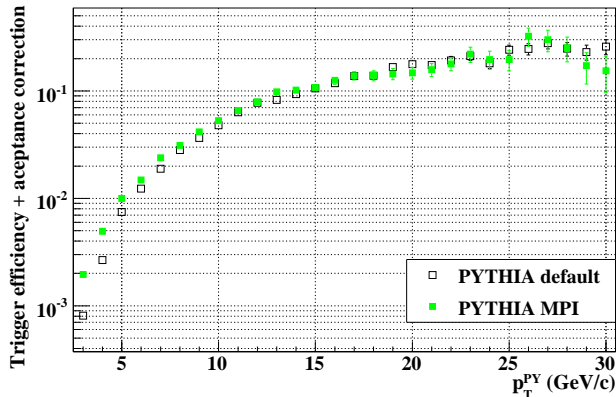


FIG. 15: (color online) The correction factor $\epsilon_{trig+acc}^j$ for high- p_T photon trigger efficiency and acceptance effect. The PYTHIA default (**black**) and the PYTHIA MPI setting (**green**) were used.

To estimate a systematic error related to the simulation reproducibility of high- p_T photon, we evaluated, in both the real data and the simulations, the ratio (r) of the reconstructed-jet yields in the high- p_T photon triggered sample to that in the MB triggered sample. The r of the PYTHIA MPI output is 5% at $p_T^{reco} = 4$ GeV/ c and 50% at $p_T^{reco} = 12$ GeV/ c , and is consistent with that of the real data within $\pm 10\%$. Therefore a 10% error was assigned to the jet production rate calculated with the PYTHIA MPI simulation. The r of the PYTHIA default output is smaller by 20-30% than that of the real data.

3. Result

Figure 16 shows the jet production rate. The main systematic errors are listed in Tab. III. The main uncer-

tainties of the measurement are the BBC cross section and the EMCAL energy scale. These errors are fully correlated bin-to-bin. The error on the EMCAL energy scale includes both the change of p_T of individual photons and the change of the threshold of the high- p_T photon requirement. In comparing the measurement and the calculation, the 10% p_T scale uncertainty of the jet definitions in the PYTHIA simulation and the NLO pQCD theory makes a 30% error at low p_T or 70% at high p_T , and is the largest source. The uncertainty of the renormalization and factorization scales in the NLO jet production cross section makes a 30% error. The calculation with PYTHIA MPI agrees with the measurement within errors over the measured range $4 < p_T^{reco} < 15$ GeV/ c .

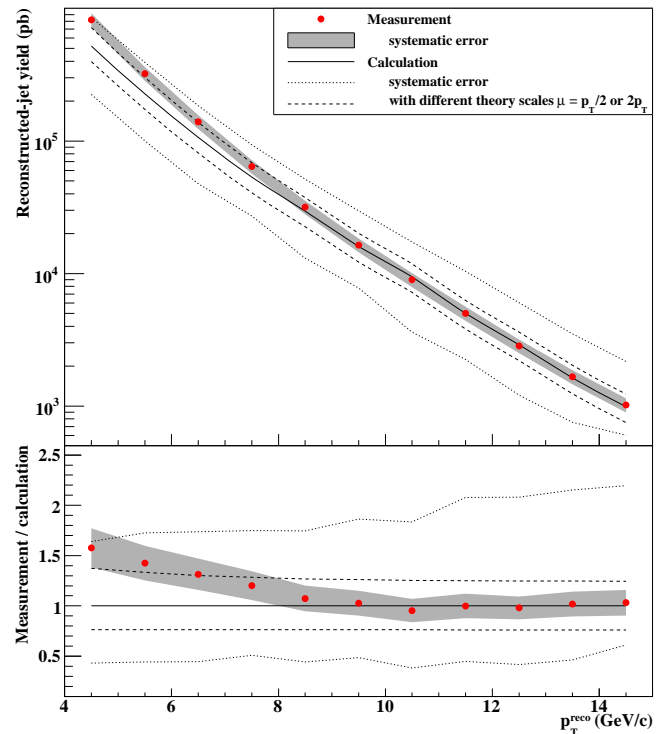


FIG. 16: (color online) (top) Reconstructed jet yield and (bottom) the ratio of the real data to the calculations. (red points) Real data with the (gray band) experimental systematic error. (black curves) PYTHIA MPI calculation with theory factorization scales of (solid curve) p_T , (upper dashed curve) $p_T/2$, and (lower dashed curve) $2p_T$. (dotted curves) Variation caused by 10% p_T scale uncertainty around the calculation. Statistical uncertainties are smaller than the size of the points.

The result with PYTHIA default is smaller than the result with PYTHIA MPI by 50% at $p_T^{reco} = 4$ GeV/ c , by 35% at $p_T^{reco} = 9$ GeV/ c and by 20% at $p_T^{reco} = 14$ GeV/ c . It can be fully explained by the difference visible in Fig. 15 between PYTHIA default and PYTHIA MPI. According to the comparisons of the event structure, PYTHIA MPI reproduces the spatial distribution of particle momenta in one event much better than the PYTHIA default. Therefore, for the jet production rate evaluated

TABLE III: Main systematic errors of the jet production rate.

Source	Size	Size on rate
Measurement		
Luminosity	9.7%	9.7%
EMCal energy scale	1.5%	7-6%
Tracking momentum scale	1.5%	0-3%
Calculation		
Jet definition	10% in p_T	30-70%
Jet shape & underlying event	-	50-20%
High- p_T photon fragmentation	-	10%
Simulation statistics	-	2-5%

with PYTHIA MPI simulation, the error due to possible insufficient tunings of PYTHIA MPI should be smaller than the difference of the jet production rate between the PYTHIA MPI simulation and the PYTHIA default simulation.

C. Double helicity asymmetry A_{LL}

1. Evaluation method (measurement)

A_{LL} is expressed with measured quantities as

$$A_{LL} = \frac{1}{|P_B||P_Y|} \frac{(N_{++} + N_{--}) - R(N_{+-} + N_{-+})}{(N_{++} + N_{--}) + R(N_{+-} + N_{-+})} \quad (12)$$

$$R \equiv \frac{L_{++} + L_{--}}{L_{+-} + L_{-+}}, \quad (13)$$

where N_{++} etc. are reconstructed-jet yields with colliding proton beams having the same ($++$ or $--$) and opposite ($+-$ or $-+$) helicity; P_B and P_Y are the beam polarizations; R is the relative luminosity, i.e. the ratio of the luminosity with the same helicity ($L_{++} + L_{--}$) to that with the opposite helicity ($L_{+-} + L_{-+}$). A_{LL} is measured fill-by-fill and the results are fit to a constant, because the beam polarization and the relative luminosity are evaluated fill-by-fill to decrease systematic errors. The average fill length was about five hours. The integrated luminosity used was 2.1 pb^{-1} . It is 0.1 pb^{-1} less than the statistics used in the production rate measurement because the data with bad conditions on the beam polarization were discarded.

The relative luminosity at PHENIX was evaluated with the MB trigger counts (N_{MB}^{++} and N_{MB}^{+-}) as $R = N_{MB}^{++}/N_{MB}^{+-}$. A possible spin dependence of MB-triggered data causes an uncertainty on the relative luminosity. The error has been checked by comparing the relative luminosity with another relative luminosity defined with the ZDCLL1 trigger counts. The ZDCLL1 trigger is fired when both the north ZDC and the south ZDC have a hit

and the reconstructed z -vertex is within 30 cm of the collision point.

The beam polarizations were measured with the pC and H-jet polarimeters [24, 25] at the 12 o'clock interaction point on the RHIC ring. One of the colliding beam rotating clockwise is called ‘‘blue beam’’, and the other rotating counterclockwise ‘‘yellow beam’’. The luminosity-weighted-average polarizations are 50.3% for the blue beam and 48.5% for the yellow beam. The sum of statistical and systematic errors on $\langle P_B \rangle \langle P_Y \rangle$ is 9.4%.

2. Evaluation method (prediction)

Polarized/unpolarized cross sections of jet production for every subprocess ($q + q$, $q + g$ and $g + g$) were calculated at NLO based on the SCA with a cone size of $\delta = 1.0$. The polarized cross sections were calculated using various $\Delta G(x)$ in order to compare the measured A_{LL} with various predicted A_{LL} 's and find the most-probable $\Delta G(x)$. Figure 17 shows the distributions of the $\Delta G(x)$ used, and the integrated values are

$$\int_0^1 dx \Delta G(x, \mu^2 = 0.4 \text{ GeV}^2) = \begin{cases} -1.24 (\Delta G = -G), \\ -1.05, \\ -0.90, \\ -0.75, \\ -0.60, \\ -0.45, \\ -0.30, \\ -0.15, \end{cases} \begin{cases} 0 (\Delta G = 0), \\ 0.24 (\text{GRSV} - \text{std}), \\ 0.30, \\ 0.45, \\ 0.60, \\ 0.70, \\ 1.24 (\Delta G = G) \end{cases} \quad (14)$$

Each $\Delta G(x)$ (except the GRSV-std, the $\Delta G = G$ input, the $\Delta G = 0$ input and the $\Delta G = -G$ input) have been obtained by refitting the GRSV parameters to the DIS data which were used in the original GRSV analysis [26]. It is noted that the DIS data used in GRSV are the data up to the year 2000 and thus are much less than that used in the updated analysis, DSSV [27], for example. The polarized PDF in the GRSV parameterization is of the form:

$$\Delta f(x, \mu_0^2) = N_f x^{\alpha_f} (1-x)^{\beta_f} f(x, \mu_0^2)_{\text{GRV}}, \quad (15)$$

where f is u , d , \bar{q} or G ; $\mu_0^2 = 0.4 \text{ GeV}^2$ is the initial scale at which the functional forms are defined as above; $f(x, \mu_0^2)_{\text{GRV}}$ is the unpolarized PDF of the GRV98 analysis [28]; N_f , α_f and β_f are free parameters. In the refit of the DIS data, the integral value of $\Delta G(x)$ from $x = 0$ to 1 was fixed to its particular value listed above, and the shape of $\Delta G(x)$ and the quark-related parameters were made free. The χ^2 of the refitting to the DIS data is 170 for the 209 data points [26] when the integral of ΔG is 0 at the initial μ^2 , for example. In the remainder of this

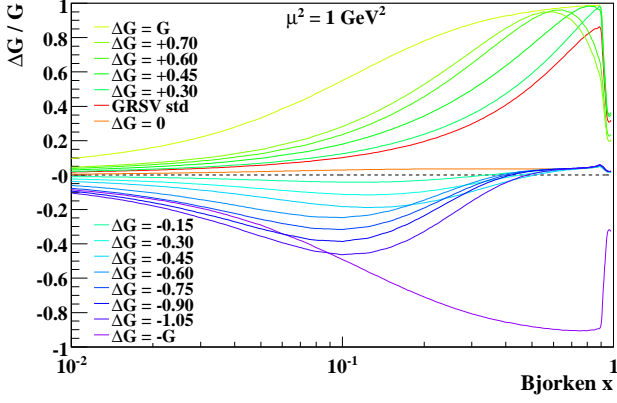


FIG. 17: (color online) Assumed gluon distribution functions at $\mu^2 = 1 \text{ GeV}^2$. The integral $\int_0^1 dx \Delta G(x)$ of each distribution at the initial scale $\mu^2 = 0.4 \text{ GeV}^2$ is, from bottom to top at $x = 0.15$, -1.24 ($\Delta G = -G$), -1.05 , -0.90 , -0.75 , -0.60 , -0.45 , -0.30 , -0.15 , 0 ($\Delta G = 0$), 0.24 (GRSV-std), 0.30 , 0.45 , 0.60 , 0.70 and 1.24 ($\Delta G = G$).

paper we concentrate on investigating the χ^2 of the six data points of the reconstructed-jet A_{LL} .

The various $\Delta G(x)$ above were evolved up to a scale μ of every event in the A_{LL} calculation. The A_{LL} of every subprocess (A_{LL}^{q+q} , A_{LL}^{q+g} and A_{LL}^{g+g}) can be derived as functions of p_T^{NLO} from the unpolarized and polarized cross sections. The PYTHIA+GEANT simulation produces the relative yields of every subprocess ($n^{q+q}(p_T^{\text{NLO}}, p_T^{\text{reco}})$, $n^{q+g}(p_T^{\text{NLO}}, p_T^{\text{reco}})$ and $n^{g+g}(p_T^{\text{NLO}}, p_T^{\text{reco}})$), as shown in Fig. 5. $A_{LL}^{\text{reco}}(p_T^{\text{reco}})$ is calculated as a mean of A_{LL}^{q+q} , A_{LL}^{q+g} and A_{LL}^{g+g} weighted by the fractions of events:

$$A_{LL}^{\text{reco}}(p_T^{\text{reco}}) = \frac{\int dp_T^{\text{NLO}} \sum_{\text{isub}} n^{\text{isub}}(p_T^{\text{NLO}}, p_T^{\text{reco}}) \cdot A_{LL}^{\text{isub}}(p_T^{\text{NLO}})}{\int dp_T^{\text{NLO}} \sum_{\text{isub}} n^{\text{isub}}(p_T^{\text{NLO}}, p_T^{\text{reco}})}, \quad (16)$$

where *isub* is $q+q$, $q+g$ and $g+g$. As an estimation of systematic errors, the slope of jet yields and the fraction of subprocesses were compared between the theory calculation and the PYTHIA simulation. Note that both the slope and the fraction that we compared have not been biased by the high- p_T photon and the small cone, since the theory calculation cannot provide biased values. The variations of A_{LL}^{reco} caused by both the slope difference and the fraction difference are negligible in comparison with other errors.

3. Result

Figure 18 shows measured A_{LL}^{reco} and four prediction curves. Table IV shows the values of measured A_{LL}^{reco} . The measured A_{LL} is consistent with zero, as the

$\chi^2/\text{n.d.f.}$ between the data points and zero asymmetry ($A_{LL} = 0$) is 1.3/6. The systematic error of the relative luminosity is much smaller than the statistical error on A_{LL} and is negligible. On the prediction curves the systematic error related to the fractions of subprocesses are smaller than the 10% p_T scale uncertainty by roughly an order of magnitude. Therefore it is not included in this plot.

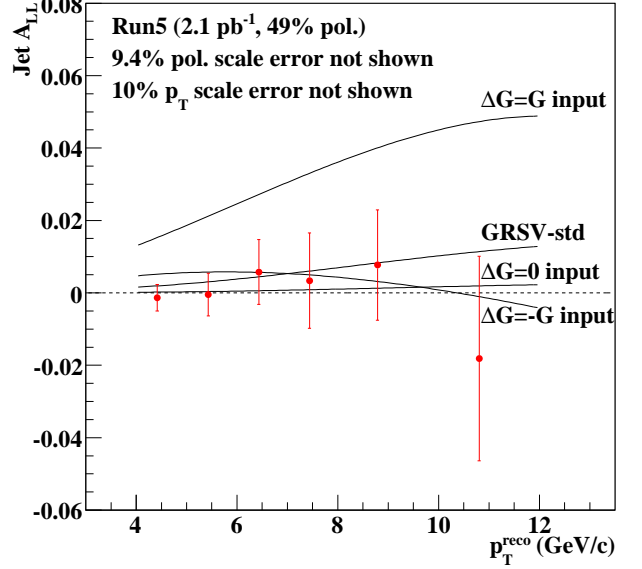


FIG. 18: (color online) Reconstructed-jet A_{LL} as a function of p_T^{reco} . (red points) Measurement with statistical error bars. (black lines) Calculation based on four $\Delta G(x)$ functions and the PYTHIA MPI + GEANT simulation.

TABLE IV: Measured reconstructed-jet A_{LL} .

p_T^{reco} range and mean (GeV/c)	A_{LL}	stat error
4-5, 4.42	-0.0014	0.0037
5-6, 5.43	-0.0005	0.0059
6-7, 6.43	0.0058	0.0089
7-8, 7.44	0.0034	0.0132
8-10, 8.79	0.0077	0.0152
10-12, 10.81	-0.0181	0.0282

It has been confirmed with a “bunch shuffling” method that the size of the statistical errors assigned is appropriate. In this method, the helicity of every beam bunch was newly assigned at random and A_{LL}^{reco} was evaluated again. Repeating this random assignment produced a large set of A_{LL}^{reco} values. Its mean value should be of course zero and was confirmed in this exercise. Its standard deviation indicates the size of the statistical fluctuation, and was consistent with the statistical errors assigned. The point-to-point variance seems smaller than the statistical errors of the data points, but we could not find any

unrecognized cause such as a statistical correlation. We conclude that the small variance of the data points happened statistically despite its small probability.

As a systematic error check, the single spin asymmetry A_L was measured. It is defined as

$$A_L \equiv \frac{\sigma_+ - \sigma_-}{\sigma_+ + \sigma_-} = \frac{1}{P} \frac{N_+ - R N_-}{N_+ + R N_-}, \quad R \equiv \frac{L_+}{L_-}, \quad (17)$$

where N_+ and N_- are reconstructed-jet yields with one colliding proton beam having the positive and negative helicity, respectively; P is the beam polarization; R is the relative luminosity, i.e. the ratio of the luminosity with the positive helicity (L_+) to that with the negative helicity (L_-). As the jets are produced via the strong force, A_L must be zero under the parity symmetry. Thus any non-zero value indicates systematic errors.

Figure 19 shows measured A_L . A_L was measured for the polarization of one colliding beam while the other beam was assumed to be unpolarized. No significant asymmetry was observed.

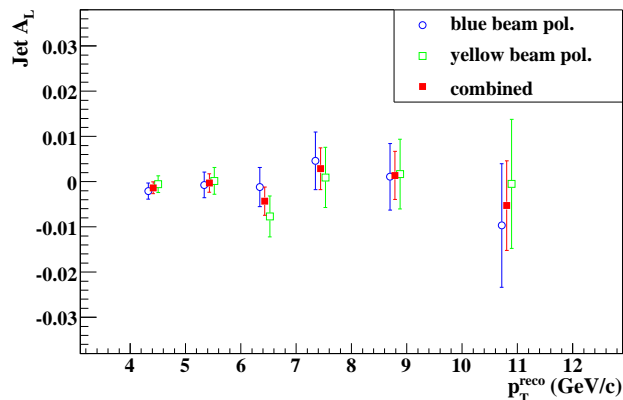


FIG. 19: (color online) Jet A_L as a function of p_T^{reco} . The blue and green points are the results using the polarizations of the blue beam and the yellow beam, respectively. The red points are the averages of the blue and green points.

4. Constraint on ΔG

To determine the range of x_{gluon} probed by this measurement, the PYTHIA MPI simulation without GEANT was used to obtain event-by-event x_{gluon} (one value per q-g scattering event, two values per g-g, or none per q-q) and also μ^2 . Figure 20 and 21 show the distributions of x_{gluon} and μ^2 , respectively. The x_{gluon} value where the yield is half maximum is 0.02 at the lower side of the “ $4 < p_T^{\text{reco}} < 5$ ” distribution and 0.3 at the upper side of the “ $10 < p_T^{\text{reco}} < 12$ ” distribution. Therefore we adopt a range of $0.02 < x_{gluon} < 0.3$ as the range probed by this measurement. Table V shows the integral of $\Delta G(x)$ at the measured x_{gluon} range, below the range and above the range. The measured x_{gluon} range includes $\sim 70\%$ of

distributions in all the four GRSV models shown. With the same procedure, the μ^2 range probed was estimated to be $5 < \mu^2 < 300 \text{ GeV}^2$.

TABLE V: Partial integral of $\Delta G(x)$ at $\mu^2 = 1 \text{ GeV}^2$.

Model	$\int dx \Delta G(x)$ at each x range			
	10^{-4} -0.02	0.02-0.3	0.3-1	10^{-4} -1
$\Delta G = -G$ input	-0.406 (24%)	-1.09 (64%)	-0.208 (12%)	-1.71
$\Delta G = 0$ input	0.00808 (10%)	0.0644 (79%)	0.00869 (11%)	0.0812
GRSV-std	0.0684 (16%)	0.258 (60%)	0.102 (24%)	0.427
$\Delta G = G$ input	0.427 (23%)	1.22 (65%)	0.226 (12%)	1.87

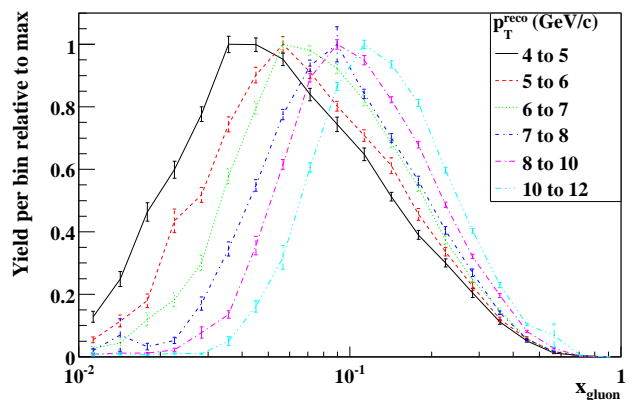


FIG. 20: (color online) Distributions of x_{gluon} in events that include a reconstructed jet with $4 < p_T^{\text{reco}} < 12 \text{ GeV}/c$.

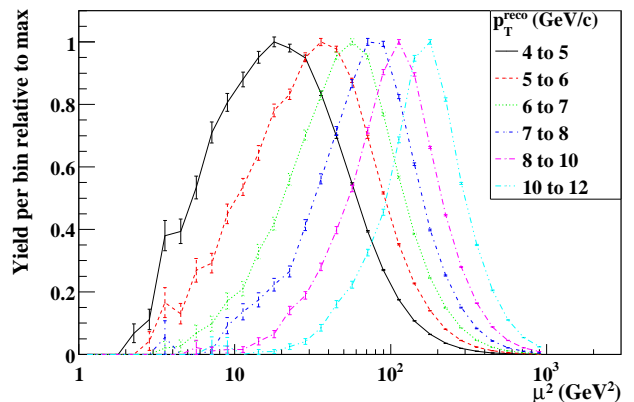


FIG. 21: (color online) Distributions of μ^2 in events that include a reconstructed jet with $4 < p_T^{\text{reco}} < 12 \text{ GeV}/c$.

Figure 22 shows the χ^2 between the 6 data points and the prediction curves as a function of the integral

$\int_{0.02}^{0.3} dx \Delta G(x, \mu^2 = 1)$ for each prediction curve. The value of μ^2 ($= 1 \text{ GeV}^2$) has been arbitrarily chosen in order to show the value of the ΔG integral in horizontal axis. Actual μ^2 used in the A_{LL} calculation varies depending on jet p_T .

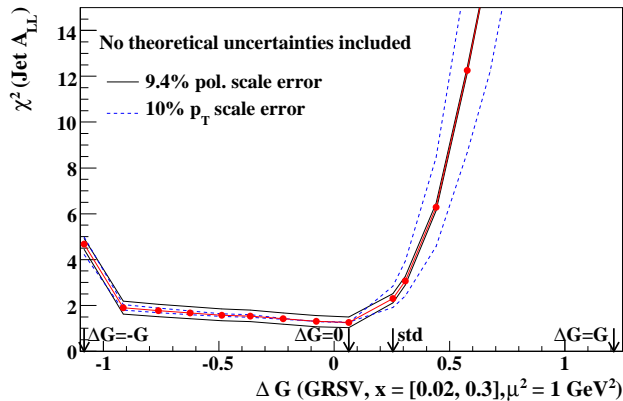


FIG. 22: (color online) χ^2 between the measured A_{LL} and the calculated A_{LL} as a function of the integrated value of $\Delta G(x)$.

The minimum of the χ^2 is ~ 1.5 at $\Delta G = 0.07$, namely the GRSV $\Delta G = 0$ input. The 95% and 99% confidence limits are where the χ^2 increases from the minimum by 4 and 9, respectively. We obtained

$$-1.1 < \int_{0.02}^{0.3} \Delta G^{GRSV}(x, \mu^2 = 1) < 0.4 \quad (18)$$

at 95% confidence level and

$$\int_{0.02}^{0.3} \Delta G^{GRSV}(x, \mu^2 = 1) < 0.5 \quad (19)$$

at 99% confidence level. In the assumptions of the present approach, the error correlations between the normalization parameter and the shape parameters in $\Delta G(x)$ are not included. Also the fact that the shape of the polarized PDFs is parameterized into Eq. 15 may cause additional uncertainty in $\Delta G(x)$.

V. CONCLUSION

We measured the event structure and the double helicity asymmetry (A_{LL}) in jet production at midrapidity ($|\eta| < 0.35$) in longitudinally polarized $p + p$ collisions at $\sqrt{s} = 200 \text{ GeV}$ were measured. The main motivation is to use this complementary approach to inclusive measurements to better understand the contribution of the gluon spin (ΔG) to the proton spin. Because this measurement of A_{LL} observes a larger fraction of the jet momentum, it reaches higher p_T and thus higher gluon x .

The MPI-enhanced PYTHIA simulation agrees well with the real data in terms of the event structure: the multiplicity of photons and charged particles, the p_T density as a function of the azimuthal angle from trigger photon, and the thrust in the PHENIX Central Arm. A small difference in the intra-jet structure, namely the fractions of photons and charged particles in jets, was observed as shown in Fig. 11(c) to (f). Nevertheless, the simulation well reproduces the shape of jets and the underlying event at this collision energy.

In the measurement of jet A_{LL} , measured particles were clustered by the seed-cone algorithm with a cone radius $R = 0.3$. The relation between p_T^{NLO} and p_T^{reco} was evaluated with PYTHIA and GEANT. The jet production rate was measured and satisfactorily reproduced by the calculation based on the NLO pQCD jet production cross section and the simulation. The jet A_{LL} was measured at $4 < p_T^{\text{reco}} < 12 \text{ GeV}/c$. The main systematic errors are a p_T scale uncertainty of 10% and a beam polarization uncertainty of 9.4%. The x_{gluon} range probed by this jet measurement with $4 < p_T^{\text{reco}} < 12 \text{ GeV}/c$ is mainly $0.02 < x < 0.3$ according to the simulation. The measured A_{LL} was compared with the predicted values based on the GRSV parameterization, and the comparison imposed the limit $-1.1 < \int_{0.02}^{0.3} dx \Delta G^{GRSV}(x, \mu^2 = 1) < 0.4$ at 95% confidence level or $\int_{0.02}^{0.3} dx \Delta G^{GRSV}(x, \mu^2 = 1) < 0.5$ at 99% confidence level. The theoretical uncertainties such as the parameterization of the polarized PDFs were not included in this evaluation.

ACKNOWLEDGMENTS

We thank the staff of the Collider-Accelerator and Physics Departments at Brookhaven National Laboratory and the staff of the other PHENIX participating institutions for their vital contributions. We also thank Werner Vogelsang for helpful discussions and calculations. We acknowledge support from the Office of Nuclear Physics in the Office of Science of the Department of Energy, the National Science Foundation, Abilene Christian University Research Council, Research Foundation of SUNY, and Dean of the College of Arts and Sciences, Vanderbilt University (U.S.A), Ministry of Education, Culture, Sports, Science, and Technology and the Japan Society for the Promotion of Science (Japan), Conselho Nacional de Desenvolvimento Científico e Tecnológico and Fundação de Amparo à Pesquisa do Estado de São Paulo (Brazil), Natural Science Foundation of China (People's Republic of China), Ministry of Education, Youth and Sports (Czech Republic), Centre National de la Recherche Scientifique, Commissariat à l'Énergie Atomique, and Institut National de Physique Nucléaire et de Physique des Particules (France), Ministry of Industry, Science and Technologies, Bundesministerium für Bildung und Forschung, Deutscher Akademischer Aus-

tausch Dienst, and Alexander von Humboldt Stiftung (Germany), Hungarian National Science Fund, OTKA (Hungary), Department of Atomic Energy (India), Israel Science Foundation (Israel), National Research Foundation and WCU program of the Ministry Education Science and Technology (Korea), Ministry of Education and

Science, Russia Academy of Sciences, Federal Agency of Atomic Energy (Russia), VR and the Wallenberg Foundation (Sweden), the U.S. Civilian Research and Development Foundation for the Independent States of the Former Soviet Union, the US-Hungarian NSF-OTKA-MTA, and the US-Israel Binational Science Foundation.

-
- [1] J. Ashman et al. (European Muon Collaboration), *Phys. Lett.* **B206**, 364 (1988).
- [2] J. Ashman et al. (European Muon Collaboration), *Nucl. Phys.* **B328**, 1 (1989).
- [3] A. Airapetian et al. (HERMES Collaboration), *Phys. Rev. D* **75**, 012007 (2007).
- [4] PYTHIA 6.2 Physics and Manual, hep-ph/0108264.
- [5] R. Field (CDF Collaboration), *Acta Phys. Polon.* **B36**, 167 (2005).
- [6] A. Adare et al. (PHENIX Collaboration), *Phys. Rev. D* **79**, 012003 (2009).
- [7] A. Adare et al. (PHENIX Collaboration), *Phys. Rev. Lett.* **103**, 012003 (2009).
- [8] B. I. Abelev et al. (STAR Collaboration), *Phys. Rev. Lett.* **100**, 232003 (2008).
- [9] K. Adcox et al. (PHENIX Collaboration), *Nucl. Instrum. Meth.* **A499**, 469 (2003).
- [10] M. Allen et al. (PHENIX Collaboration), *Nucl. Instrum. Meth.* **A499**, 549 (2003).
- [11] C. Adler et al., *Nucl. Instrum. Meth.* **A470**, 488 (2001).
- [12] A. Bazilevsky et al., *Phys. Lett.* **B650**, 325 (2007).
- [13] A. Adare et al. (PHENIX Collaboration), *Phys. Rev. D* **76**, 051106 (2007).
- [14] L. Aphecetche et al. (PHENIX Collaboration), *Nucl. Instrum. Meth.* **A499**, 521 (2003).
- [15] K. Adcox et al. (PHENIX Collaboration), *Nucl. Instrum. Meth.* **A499**, 489 (2003).
- [16] J. T. Mitchell et al. (PHENIX Collaboration), *Nucl. Instrum. Meth.* **A482**, 491 (2002).
- [17] GEANT 3.2.1 Manual (1994), URL <http://wwwasdoc.web.cern.ch/wwwasdoc/pdfdir/geant.pdf>.
- [18] R. Field (CDF Collaboration) (2003), URL <http://www-cdf.fnal.gov/physics/new/qcd/run2/ue/chgjet/>.
- [19] G. Alexander et al. (OPAL Collaboration), *Phys. Lett.* **B265**, 462 (1991).
- [20] R. Akers et al. (OPAL Collaboration), *Z. Phys.* **C68**, 179 (1995).
- [21] F. Aversa, M. Greco, P. Chiappetta, and J. P. Guillet, *Z. Phys.* **C46**, 253 (1990).
- [22] B. Jager, M. Stratmann, and W. Vogelsang, *Phys. Rev. D* **70**, 034010 (2004), hep-ph/0404057.
- [23] W. Vogelsang calculation, private communication.
- [24] J. Tojo et al., *Phys. Rev. Lett.* **89**, 052302 (2002).
- [25] H. Okada et al., *Phys. Lett.* **B638**, 450 (2006).
- [26] M. Gluck, E. Reya, M. Stratmann, and W. Vogelsang, *Phys. Rev. D* **63**, 094005 (2001).
- [27] D. de Florian, R. Sassot, M. Stratmann, and W. Vogelsang, *Phys. Rev. Lett.* **101**, 072001 (2008).
- [28] M. Gluck, E. Reya, and A. Vogt, *Eur. Phys. J.* **C5**, 461 (1998).